ESTIMATING INDUCER BLADE DAMPING IN WATER WITH ON-BLADE STRAIN MEASUREMENTS*

Andrew Mulder and Stephen Skelley
NASA Marshall Space Flight Center
MSFC, AL

ABSTRACT

This paper describes the testing, methodology, and results for estimating critical damping ratios of inducer blade structural natural frequencies. A sub-scale inducer water flow test was performed with on-blade strain gauge measurements. Data were acquired in quiescent air and water, and also at several shaft speeds and operating conditions. Two methods were used to provide active excitation to the blades. The first was to impart a mechanical impulse to the inducer shaft and observe the strain gauge response. The second was to install a stator plate upstream of the inducer to create a non-uniform but regular pressure field at the inducer inlet. There are challenges with using either approach, but damping information was extracted using both methods. Results showed that the critical damping ratio for a given blade mode increased from air to quiescent water, and also increased when the inducer was spinning.

INTRODUCTION

A typical finite element based forced response analysis is comprised of a harmonic forcing function applied to a structural model with an assumed damping factor to generate frequency response functions over a given driving frequency range. The magnitude and phase of the structural response to the forcing function depends directly on what structural natural frequencies are present in the driving frequency range, and also on the damping factor that is used for the response analysis. The damping factor is intended to represent the dissipation of energy from an oscillating structure. For a single degree of freedom system modeled with viscous damping (i.e. a force proportional to velocity, opposed to the direction of velocity) the critical damping factor is:

$$c_c = 2m\omega_n$$

where m is the mass of the system and ω_n is the system natural frequency. This is the damping coefficient that provides the quickest approach back to the unperturbed state. The damping factor used in the finite element analysis is often given as a percentage of c_c for a given mode, which is referred to as the critical damping ratio ζ. A heuristic approach is often taken regarding the amount of damping applied to a given structure. Thin, ‘lightly damped’ structural components often are assigned damping factors on the order of 0.1% of the critical damping factor for whatever modes are being analyzed. Those values typically represent the damping due to conversion of potential and kinetic energy within the material to thermal energy, and can be referred to as the ‘material’ or ‘structural’ damping associated with that component. Another source of damping can come from friction at joints between assembled components, which can add an additional 0.5-1% to the applied critical damping ratio depending on the nature and number of joints in the assembly.

There are also certain situations where the motion of an oscillating structure can be dissipated by forces external to the structure. For example, a thin structure moving through a viscous fluid will be subject to a drag force and other hydrodynamic phenomena such as vortex shedding. These hydrodynamic phenomena can impose loads that work against the motion of the structure. To most accurately capture these hydrodynamic effects with a FEM analysis it would require a fully coupled, high fidelity fluid/structure model. What typically is done instead is to model the structure en vacuo and account for hydrodynamic effects by simply increasing the applied critical damping ratio.

The amount of effective damping provided by hydrodynamic effects can be significantly larger (an order of magnitude or more) than the material/structural damping for thin, lightly damped, monolithic structures. Various experiments have been done to measure hydrodynamic damping over the years [2], [3]. Much of the existing work involves geometry representing gas turbine blades and bladed disks.

---

[*] Approved for public release; distribution is unlimited.

This paper describes some of the results of a water flow test of a subscale 4-bladed liquid rocket engine inducer. The test employed strain gauges mounted on the blade surfaces, and damping information was extracted at various operating conditions for some of the inducer blade structural modes. The objective of the damping testing was to provide information regarding a reasonable critical damping ratio to use when performing finite element analysis of the inducer blades at realistic operating conditions.

TEST SETUP

FACILITY

This test was performed at the Marshall Space Flight Center (MSFC) Inducer Test Loop (ITL). The facility is a closed loop with a six-inch diameter inlet section containing the test article. The rotating assembly is attached to a bearing box and sealed with a carbon shaft seal. A 150 horsepower electric motor is used to drive the rotating assembly. The facility includes a torque meter, a boost pump for fine flow control, a flow control valve for gross flow control, and a reservoir/ullage tank for controlling the system static pressure. Water temperature is controlled with a chiller loop that can tap off the main loop, and dissolved oxygen content can be controlled with a degassing unit. See Figure 1 for a photograph of the facility.

A number of steady state parameters were recorded on the data system including a reference inlet total pressure, the inducer head rise, shaft speed, flow rate, water temperature, and torque. These parameters were used to relate dynamic data to the steady operating conditions.

Dynamic data were acquired using a 128 channel system with VXI Technology VT1432A A/D boards. Data were sampled at 20480 samples per second per channel.

INSTRUMENTATION

The test included multiple static and fluctuating pressure measurements throughout the facility. The inducer was also instrumented with 12 strain gauges. The strain gauges used in this test were Vishay Micro-Measurements Model CEA-06-062UB-350 (2). They were installed on the suction side of the blades and were aligned to sense strain in the blade hub to tip direction. To improve survivability the gauges were waterproofed and covered with metal foil (Figure 3). Each gauge was part of a three-wire quarter bridge Wheatstone bridge circuit. Each of the 12 bridges was completed with a Micro-Measurements MR1-350-130 bridge completion module. The bridges were powered by Michigan Scientific AMP-SG-MH amplifiers, which also provided a gain to the bridge output. The amplifiers and bridge completion modules were mounted on a disk which was attached to the ITL shaft (Figure 4). Power to the amplifiers and the amplified bridge output signals were routed through a Michigan Scientific SR20M slip ring.

During installation of the test article into the facility, one of the strain gauge bridges was damaged, so viable data were collected from 11 of the twelve gauges.

DAMPING ESTIMATION METHODOLOGY

Prior to the water flow test, a modal test was performed on the instrumented inducer [4] in air and water to identify the frequency range over which to expect inducer modes. The results of the survey indicated fundamental blade bending modes in air around 3-5 kHz and 1-3 kHz in water.

For the water flow test, damping was estimated using both frequency response function (FRF) based analysis and impulse response function (IRF) based analysis. The test process and damping estimation methods for each analysis are described in detail below.

With the inducer installed in the facility but not filled with water, the impulse response method was employed to measure blade damping in quiescent air. Then then the facility was filled with water and the impulse response method was used to measure damping in quiescent water. Then the inducer was spun at three different shaft speeds over a range of cavitation number (i.e. dimensionless inlet pressure) and flow coefficient (i.e., dimensionless flow velocity), and the impulse response method was again employed to measure blade damping. The frequency response function method required flowing water so it was not used to measure damping at any quiescent conditions, but testing with this method was performed over various speed ranges and flow coefficients.

IMPULSE RESPONSE BASED ANALYSIS

The impulse response methods involves imparting an impulse to the system to excite the structural modes and measuring the frequency and decay rate of the response. Ideally the impulse would be applied directly to the structure of interest, i.e., the inducer blades. However with the spinning inducer this was not possible and instead, a remote controlled hammer (PCB 086C09 Electric Hammer, Figure 5) was used to strike an exposed section of the test rig shaft between the aft-most bearing and the torque meter (Figures 6 and 7). The mechanical impulse is transmitted to the blades through the shaft and the resulting blade strain response is recorded. This process is referred to as a 'ping' test.

The resulting strain data is analyzed using a digital bandpass filter on the impulse response data around the frequency content of interest and extracting the amplitude envelope from the filtered data. Assuming the structure responds like an underdamped single degree of freedom system with natural circular frequency ω_n and critical damping ratio ζ, where $0 \leq \zeta \leq 1$, the impulse response $\mu(t)$ at the damped natural circular frequency $\omega_d = \omega_n\sqrt{1-\zeta^2}$ is given by:

$$\mu(t) = Ae^{-\zeta\omega_n t}cos(\omega_d t + \phi)$$

The value of the constants A and ϕ depends on the impulse strength and system initial conditions. The envelope amplitude X_E can be used to estimate damping.

$$X_E(t) = Ae^{-\zeta\omega_n t} = Ae^{-\frac{\zeta\omega_d}{\sqrt{1-\zeta^2}}t}$$

The envelope amplitude can be calculated from $\mu(t)$ with an instantaneous frequency and amplitude demodulation method, wavelet transform methods, or the Hilbert transform. Taking the logarithm of both sides of the above equation results in an equation that is linear with time:

$$log[X_E(t)] = -\frac{\zeta\omega_d}{\sqrt{1-\zeta^2}}t + log[A]$$

This equation has the form $y = -\beta t + b$, with:

$$\beta = \frac{\zeta\omega_d}{\sqrt{1-\zeta^2}}$$

Therefore damping can be estimated by fitting the log of the amplitude envelope to a straight line and using the slope β and the frequency of the oscillation ω_d:

$$\zeta = \frac{1}{\sqrt{1+(\omega_d/\beta)^2}} \tag{1}$$

PING TEST DAMPING EXTRACTION

There were approximately 40 dynamic data ping test files, each with 11 viable strain gauge channels, with 5-9 operating condition set points per file (Figure 8), and 10 pings per set point. This added up to thousands of strain impulse responses to analyze. A Matlab script was developed using the discrete Fourier transform (DFT) to identify the ping frequency content, and digital filters coupled with a frequency modulation technique to calculate instantaneous amplitude and frequency. The script executed the following process on each dynamic data file:

1. Each ping event is identified in the dynamic data file using either the strain gauges themselves or an accelerometer mounted on the electric hammer or bearing box.
2. An 8192-point block of raw data around the ping event is selected for each gauge and a high pass (1kHz) filter is applied.
3. A 2048-point DFT centered around the ping event is computed.
4. The largest DFT amplitude peak frequencies (up to three) from each gauge are selected for the instantaneous calculation.
5. The instantaneous calculation is performed on each target frequency, yielding the amplitude envelope and instantaneous frequency of the ping, sample by sample.
6. For each envelope, the peak amplitude is found, and an interval starting at that peak and ending where the slope of the envelope becomes positive for either the first or second time (i.e., no longer decaying, see notes below) is defined.
7. The interval defined above is checked for length. If the interval is longer than 7 cycles of the average frequency over that interval, the process continues. Otherwise, the interval is discarded and no damping is calculated for that bridge during the ping event.
8. If the interval meets the duration requirement, a straight line is fit to the log of the amplitude over the interval defined above. The standard estimate of error (σ_r) is calculated from the residuals of the fit.
9. The slope of the linear regression and the average instantaneous frequency are used in Equation 1 to estimate damping.
10. The damping value, average frequency, and σ_r from the above calculation are saved for that bridge for that ping event.
11. The operating conditions over the ping event interval are also saved

Some notes regarding the above process:

- The high pass filter applied at the start of the process is a kaiser window finite impulse response (FIR) digital filter with a stop-band at 750 Hz and pass-band at 1000 Hz, with 60dB attenuation and 0.01 dB pass-band ripple. It was created with the Matlab *designfilt* function and applied to the data with the *filtfilt* function. This results in a twice-filtered time history with zero phase shift.
- Visual inspection of the amplitude envelopes of many ping events showed that often the decaying envelope had an inflection point where the slope of the envelope goes from negative to slightly positive, then back to negative. The interval selection process in Step 6 first selects an interval from the envelope peak to this inflection point, but if that interval does not meet the duration requirement, the slope requirement is relaxed and a new interval is defined that includes the first inflection point, ending instead at the 2^{nd} inflection point. This interval is then checked for duration and is either discarded or carried forward. This was deemed acceptable because many pings exhibited this behavior, and the negative sloped portions of these intervals had very similar slope.

- The instantaneous frequency calculation can result in erroneous frequency spikes where the atan2 function wraps phase. Therefore, if the instantaneous frequency for an envelope exceeded the pass band frequency limits of the filter used in the calculation, those frequencies were not used to calculate the average frequency over the interval.

- The standard error of the estimate σ_r is the root mean square of the curve fit residuals. Thus for an interval with N points:

  $$\sigma_r = \sqrt{\frac{1}{N}\sum_{n=1}^{N}(y_n - y'_n)^2}$$

  Where y_n is the n^{th} data point in the interval and y'_n is the value of the curve fit to that point. If the average of the residuals is zero, then σ_r is equal to the standard deviation of the residuals. This quantity is used as a weighting factor for the damping estimates, such that damping ratios derived from 'good' (low σ_r) linear fits are favored:

  $$\zeta_w = \frac{\sum_{i=1}^{N} w_i \zeta_i}{\sum_{i=1}^{N} w_i}$$

  $$w_i = \frac{1}{\sigma_{ri}^2}$$

Figures 9 and 10 demonstrate the ping test damping calculation process graphically, with one subtle exception. In Figure 10 the damping ratio shown in the plot is calculated point by point, while the actual saved value is the weighted average over the interval.

FREQUENCY RESPONSE BASED ANALYSIS

The classic frequency response function (FRF) based approach to estimating damping is to excite the system with a known input forcing function and simultaneously record the input and output. The relative magnitude and phase between the input and output is computed in the frequency domain, and is called the frequency response function. Assuming the system behaves like a single degree of freedom system, damping can be estimated according to the FRF-based methods such as the half power point or half quadratic gain method [5].

$$\zeta = \sqrt{\frac{1}{2} - \left(4 + 4\left(\frac{f_u - f_l}{f_p}\right)^2 - \left(\frac{f_u - f_l}{f_p}\right)^4\right)^{-1/2}} \tag{2}$$

where f_p is the frequency at the peak value of the transfer function, $H_{xy}(f_p) = max|H_{xy}(f)|$ and f_u, f_l are the frequencies above and below f_p where $|H_{xy}(f_{u,l})|^2 = 0.5|H_{xy}(f_p)|^2$.

In this test series, two approaches/variations on the above description were attempted, and are described below.

PASSIVE EXCITATION FRF

The most simple approach was to identify blades modes excited by the random variation in flow, i.e. background noise. If a structural mode could be identified, a pseudo-FRF was calculated where the input was assumed to be planar (k=0) pressure field in plane 1000. Once a transfer function $H_{xy}(f)$ is computed the damping ratio can be estimated using the half gain quadratic formula.

A challenge with the passive excitation FRF method is identifying structural modes. Since the method relies on ambient noise levels, there is no control on forcing function amplitude in a given frequency range. Therefore, some modes may not be observed due to low excitation levels or may have very low signal to noise ratios making them difficult to identify.

As a matter of fact, when operating around the nominal hydrodynamic conditions, there did not appear to be any randomly induced strain responses in the frequency range of interest, based on the modal results in [4]. Higher frequency modes did appear to respond, but due to lack of response around where the fundamental bending modes of the blades were expected to occur, this method was substituted for an active excitation source method.

STATOR PLATE EXCITATION FRF

The other FRF based approach was to install a stator plate just upstream of the inducer. The desired effect of the plate was to produce wakes that created a time-stationary, spatially periodic pressure/flow field at the inducer inlet. The inducer blades would pass through these wakes and experience a forcing function with a fundamental frequency equal to the shaft speed times the number of stators. For example, with a 9-vane stator plate, an inducer blade will pass through 9 wakes per revolution and thus experience a 9N forcing function. The forcing function frequency is then swept across a targeted frequency range and the resulting strain response as a function shaft speed can be used to make a pseudo-FRF.

A challenge for this approach is measuring the input. A true FRF would require on-blade pressure measurements, which did not exist. And the fluctuating pressure measurements in the duct walls do not detect the pressure field induced by the stator wakes because the forcing function is not rotating. Additionally, there were not enough static pressure measurements to accurately determine the amplitude of the static pressure distribution near the inducer inlet. To overcome this, it is assumed that the wake strength is proportional to the inlet dynamic pressure, i.e., the square of the inlet flow velocity, which is a measured quantity. The pseudo-FRF $\hat{H}_{xy}$ for this kind of test can be built by tracking the strain response ϵ' of the speed dependent, stator wake-induced forcing function as a function of frequency, normalized by the inlet dynamic pressure. Damping can then be estimated with the half quadratic gain method.

$$\hat{H}_{xy} = \frac{\epsilon'}{\frac{1}{2}\rho c_m^2}$$

Based on the ping test data and a previous modal test [4], along with consideration for facility capacity, the maximum frequency targeted for a stator plate frequency sweep was approximately 2300 Hz. The facility operating speed was initially limited to 5000 RPM. Therefore, a forcing function at approximately 27 times shaft speed was needed to reach the maximum target frequency. Two design approaches were tried. First, a nine-vane stator plate was tested, at two axial locations, denoted as ‘far’ and ‘close’. The far location was such that the downstream edge of the half-inch thick plate was approximately 1/3 of a duct diameter (L/D) upstream from the blade leading edge tip. The close position put the plate trailing edge approximately 1/5 L/D upstream of the leading edge plane. The 2^{nd} harmonic of the resulting 9-vaned pressure wakes was assumed to be persistent enough to provide a forcing function to the blades.

Then a 27-vaned plate was tested, where the fundamental vane pass frequency would serve as the forcing function. This was installed only in the ‘close’ axial location. Figure 11 shows a picture of each stator plate installed in the ITL.

Frequency sweeps were performed in a two different ways. For both the 9 and 27 vane testing, one method was as follows:

1. Set the inlet pressure at atmospheric (or higher) at a given flow coefficient, to avoid cavitation formation on the stator plate
2. Begin at the lowest sweep frequency, 3000 RPM
3. Increase shaft speed by approximately 200 RPM
4. Adjust flow rate if possible with the boost pump and flow control valve to maintain the same flow coefficient
5. Repeat Steps 3 and 4, ending the frequency sweep at a shaft speed of 5000 RPM

When ramping speed at relatively high flow coefficients, there was a limitation on the valve and boost pump flow control capacity. Therefore, the flow coefficient was not constant over the speed range tested when at flow coefficients above approximately 140% of the rated flow coefficient.

An additional set of data were acquired for the 27-vane configuration, where the sweep tests were performed boustrophedonically, i.e., ‘as the ox plows the field’:

1. Set the inlet pressure at atmospheric (or higher) at a given flow coefficient, to avoid cavitation formation on the stator plate.
2. Begin at the lowest sweep frequency, 3000 RPM and flow coefficient (85% rated flow)
3. Hold shaft speed constant, sweep the flow coefficient to the maximum value (140-160% rated flow)
4. Increase shaft speed by approximately 200 RPM
5. Sweep flow rate back down the minimum value
6. Increase shaft speed by approximately 200 RPM
7. Repeat steps 3 to 6 until attaining a shaft speed of 5000 rpm

For all frequency sweep data the amplitude of the strain oscillation at 27 times shaft speed (27N) was calculated and divided by the corresponding inlet dynamic pressure to give a pseudo-transfer function $\hat{H}_{xy}$.

The half power bandwidth Δ for a single degree of freedom system can be estimated using the following equation:

$$\Delta = 2\zeta\omega_n$$

For an oscillation around 1700 Hz with 3% critical damping, the half power bandwidth is approximately 100 Hz. The dwell increment of 200 RPM used during testing means that the 27N frequency increment between dwells is approximately 90 Hz. Therefore, based on the ping test results, it is highly likely that at least one frequency dwell interval occurred within the half power bandwidth for the targeted blade modes.

Figure 12 shows an example of the stator damping extraction process using the pseudo-transfer function method.

RESULTS

BLADE NATURAL FREQUENCY RESULTS

Both the ping testing and stator plate testing rely of identification the frequency at which a strain response occurs. Before proceeding with the damping results it is worth comparing the blade response frequencies from the these methods and assessing any similarities or differences in the outputs.

Figure 13 is a histogram that shows the distribution of average frequencies selected by the automated process. It shows that the (up to) three largest peaks in the ping events in the most upstream location (1^{st} column, gauges 1, 4, 7, & 10) exhibited frequency content around 2.2 kHz, 3.5 kHz, and from 4-6 kHz. In the middle position, (2^{nd} column, gauges 2, 5, 8, & 11) there were many large responses around 2.2 kHz, and also some at 3.5 kHz, and a smaller number of responses at 1 & 1.6 kHz. In the most downstream location (3^{rd} column, gauges 3, 6, & 9) the prominent responses occurred at 1, 1.6, and 2.2 kHz. To be clear, all of the frequencies described above could be found at all gauge positions, but the relative magnitude of the responses varied across position.

Blade responses from the stator plate testing are shown in Figures 24, 27, 30, and 32. The bridge arrangement is the same as described for the ping testing. A response at $\sim$1.7 kHz was detected at all bridge locations for all three stator vane configurations. A higher response at $\sim$2.2 kHz was detected simultaneously with the 1.7 kHz response, but only with the 27-vane stator installed.

These observations suggest that the two excitation methods generated blade responses consistent with the quiescent water results in [4]. However, it also suggests that the response for a particular mode may be sensitive to the excitation method.

PING TEST RESULTS

Figures 9 is an example of a strain gauge response in water. The duration of air and quiescent water test responses were observed to be on the order of 10 milliseconds, while the spinning test response durations were closer to 5 milliseconds. Operating at certain hydrodynamic conditions can also induce strains on the same order of magnitude as the hammer strikes, adding to the challenge of extracting damping ratios from the strain data. Also, in some cases, the ping responses do not follow the 'canonical' impulse SDOF response of a decaying exponential. This is likely due to the indirect way in which the blades are being excited, i.e., striking the shaft instead of the blades. In addition to that, some of the bridges simply have less than ideal grounding due to being made of small wires and difficult installation clearances, and being subject to wear and tear. These factors can degrade the signal quality. The automated procedure explained above for extracting damping ratios was set up in an attempt to reject data of poor quality and estimate damping from data of acceptable quality.

In order to highlight some characteristics of the ping data, the data from tests run at 4200 RPM are included in this section. General results from tests at other speeds are summarized in table form. Also, some of the following figures show damping, amplitude, etc over a specific frequency range, in this case 2-2.5 kHz. This was done because that frequency range was found over all bridges and at relatively high amplitudes.

Figure 14 shows the amplitude in microstrain of the prominent frequency content in each bridge. Generally, ping response amplitudes were highest in the most downstream location, reaching values as high as 50 $\mu\epsilon$. Typical amplitudes were in the 10-20 $\mu\epsilon$ range.

Figure 15 shows the critical damping ratio estimates plotted vs frequency. Damping estimates ranged significantly, going below 1% critical damping to over 8%. This variation was seen over all ping response frequency content. Figure 16 shows histograms for frequencies between 2 and 2.5 kHz, further illustrating the distribution of damping estimates.

Figure 17 contains scatter plots of ping response amplitudes for frequencies between 2 and 2.5 kHz vs estimated damping ratio. Here the data are mixed, with amplitude showing insignificant correlation in the most-upstream locations, while showing weak to moderate positive correlation ($r \approx$ 0.3 to 0.5 at $p < 0.05$) in the other locations. This result could indicate that the forcing function amplitude has an influence on damping.

Figures 18 and 19 show the σ_r-weighted average damping for frequencies between 2 and 2.5 kHz plotted against flow coefficient and cavitation number. It is difficult to detect a correlation between damping ratio and these operating conditions.

To make a broader comparison, Tables 1-9 contain some statistics for the ping test damping extraction process. Each table represents the damping (at frequencies between 2 and 2.5 kHz) over all relevant operation conditions for that configuration, i.e. air, water, or spinning in water. The high and low 95% confidence interval values, median, arithmetic mean, and σ_r-based weighted average are tabulated for each bridge and configuration, along with a blade average weighted mean. The 95% confidence intervals are estimated using the weighted damping ratio cumulative density functions from the damping ratio estimation process.

Figures 20 and 21 show some inducer average weighted mean damping ratios for each ping test configuration along with the inducer average high and low 95% confidence bounds, for 'low frequency' modes (air $\sim 3-4$ kHz, water $\sim 2-2.5$ kHz). Figure 20 shows the weighted averages over all conditions for each bridge, while Figure 21 shows the average damping and 95% confidence intervals over all conditions and bridges. The plots show that the damping ratio for what are assumed to be comparable structural modes goes up when the blades are in water as opposed to air, and then it goes up even more when the inducer is spinning. This is presumably due to the relative flow across blades when spinning and the pumping work done by the blades on the fluid, although the results do not show an obvious relationship to flow coefficient.

Table 1: Zero RPM air pings, low frequencies

Bridge	+U95	-U95	Median	Mean	Weighted Mean (ζ_w)	Blade Avg (ζ_w)
1	0.020	0.000	0.006	0.008	0.004	0.008
2	0.027	0.002	0.024	0.022	0.014	
3	0.021	0.001	0.009	0.009	0.006	
4	0.026	0.006	0.010	0.011	0.011	0.019
5	0.036	0.001	0.025	0.025	0.027	
6	0.030	0.005	0.019	0.019	0.018	
7	0.052	0.002	0.009	0.016	0.008	0.012
8	0.080	0.000	0.018	0.020	0.021	
9	0.060	0.000	0.016	0.021	0.007	
10	0.025	0.000	0.005	0.007	0.006	0.007
11	0.033	0.003	0.006	0.008	0.007	

Table 2: Zero RPM water pings, 0-2 kHz

Bridge	+U95	-U95	Median	Mean	Weighted Mean (ζ_w)	Blade Avg (ζ_w)
1	0.026	0.021	0.024	0.024	0.024	0.021
2	0.020	0.010	0.015	0.016	0.016	
3	0.049	0.004	0.015	0.020	0.024	
4	–	–	–	–	–	0.011
5	0.029	0.004	0.010	0.011	0.011	
6	0.065	0.000	0.012	0.018	0.012	
7	0.091	0.001	0.027	0.036	0.042	0.025
8	0.022	0.007	0.011	0.013	0.011	
9	0.038	0.008	0.020	0.023	0.023	
10	0.064	0.034	0.039	0.046	0.040	0.032
11	0.030	0.005	0.019	0.019	0.024	

Table 3: Zero RPM water pings, 2-2.5 kHz

Bridge	+U95	-U95	Median	Mean	Weighted Mean (ζ_w)	Blade Avg (ζ_w)
1	0.031	0.011	0.021	0.020	0.021	0.026
2	0.039	0.004	0.019	0.022	0.035	
3	0.042	0.012	0.014	0.018	0.021	
4	0.025	0.015	0.019	0.020	0.020	0.029
5	0.045	0.020	0.032	0.034	0.033	
6	0.059	0.009	0.033	0.034	0.033	
7	0.033	0.003	0.019	0.019	0.020	0.023
8	0.076	0.016	0.020	0.026	0.022	
9	0.035	0.010	0.015	0.015	0.029	
10	0.020	0.015	0.018	0.018	0.018	0.021
11	0.029	0.009	0.025	0.025	0.025	

Table 4: 2970 RPM water pings, 0-2 kHz

Bridge	+U95	-U95	Median	Mean	Weighted Mean (ζ_w)	Blade Avg (ζ_w)
1	N/A	N/A	N/A	N/A	N/A	0.038
2	0.067	0.002	0.034	0.037	0.042	
3	0.075	0.000	0.032	0.033	0.035	
4	–	–	–	–	–	0.038
5	0.077	0.007	0.027	0.029	0.033	
6	0.076	0.001	0.038	0.039	0.044	
7	–	–	–	–	–	0.045
8	0.091	0.001	0.040	0.045	0.052	
9	0.080	0.000	0.035	0.037	0.038	
10	–	–	–	–	–	0.031
11	0.057	0.002	0.027	0.027	0.031	

Table 5: 2970 RPM water pings, 2-2.5 kHz

Bridge	+U95	-U95	Median	Mean	Weighted Mean (ζ_w)	Blade Avg (ζ_w)
1	0.073	0.028	0.045	0.046	0.043	0.045
2	0.085	0.015	0.043	0.046	0.048	
3	0.079	0.014	0.041	0.044	0.044	
4	0.071	0.026	0.040	0.042	0.045	0.047
5	0.080	0.010	0.041	0.043	0.047	
6	0.082	0.007	0.040	0.043	0.050	
7	0.075	0.035	0.052	0.053	0.052	0.050
8	0.084	0.014	0.045	0.047	0.046	
9	0.090	0.015	0.044	0.047	0.051	
10	0.086	0.021	0.050	0.051	0.055	0.050
11	0.076	0.011	0.039	0.041	0.045	

Table 6: 3334 RPM water pings, 0-2 kHz

Bridge	+U95	-U95	Median	Mean	Weighted Mean (ζ_w)	Blade Avg (ζ_w)
1	–	–	–	–	–	0.033
2	0.063	0.003	0.027	0.030	0.032	
3	0.075	0.000	0.032	0.032	0.035	
4	–	–	–	–	–	0.029
5	0.057	0.002	0.021	0.022	0.019	
6	0.081	0.001	0.035	0.036	0.039	
7	–	–	–	–	–	0.037
8	0.071	0.001	0.025	0.028	0.037	
9	0.071	0.001	0.033	0.034	0.038	
10	–	–	–	–	–	0.024
11	0.063	0.003	0.025	0.028	0.024	

Table 7: 3334 RPM water pings, 2-2.5 kHz

Bridge	+U95	-U95	Median	Mean	Weighted Mean (ζ_w)	Blade Avg (ζ_w)
1	0.073	0.023	0.049	0.049	0.050	0.047
2	0.081	0.011	0.047	0.048	0.048	
3	0.081	0.011	0.042	0.044	0.041	
4	0.063	0.023	0.040	0.040	0.042	0.043
5	0.082	0.007	0.039	0.041	0.044	
6	0.087	0.002	0.039	0.041	0.044	
7	0.081	0.031	0.052	0.054	0.055	0.050
8	0.090	0.015	0.049	0.051	0.050	
9	0.093	0.008	0.042	0.046	0.045	
10	0.075	0.020	0.044	0.046	0.055	0.048
11	0.074	0.004	0.037	0.039	0.042	

Table 8: 4200 RPM water pings, 0-2 kHz

Bridge	+U95	-U95	Median	Mean	Weighted Mean (ζ_w)	Blade Avg (ζ_w)
1	0.055	0.000	0.030	0.027	0.025	0.028
2	0.070	0.000	0.021	0.024	0.029	
3	0.070	0.000	0.024	0.026	0.031	
4	0.028	0.023	0.023	0.025	0.023	0.028
5	0.060	0.000	0.021	0.023	0.025	
6	0.070	0.000	0.026	0.029	0.036	
7	0.069	0.004	0.036	0.037	0.054	0.040
8	0.070	0.000	0.027	0.028	0.034	
9	0.075	0.000	0.028	0.030	0.033	
10	0.066	0.001	0.028	0.030	0.036	0.032
11	0.060	0.000	0.022	0.024	0.029	

Table 9: 4200 RPM water pings, 2-2.5 kHz

Bridge	+U95	-U95	Median	Mean	Weighted Mean (ζ_w)	Blade Avg (ζ_w)
1	0.077	0.012	0.046	0.047	0.049	0.049
2	0.090	0.005	0.047	0.048	0.051	
3	0.092	0.002	0.043	0.045	0.046	
4	0.062	0.022	0.039	0.040	0.041	0.041
5	0.076	0.001	0.036	0.038	0.041	
6	0.081	0.001	0.035	0.038	0.041	
7	0.072	0.007	0.049	0.047	0.052	0.051
8	0.085	0.010	0.050	0.050	0.051	
9	0.088	0.008	0.047	0.047	0.051	
10	0.071	0.001	0.036	0.036	0.048	0.043
11	0.076	0.006	0.034	0.036	0.038	

STATOR PLATE RESULTS

Figures 22, 25, 28, and 31 shows the normalized flow coefficient plotted against 27 times shaft speed for the various stator test configurations.

Figure 23 is a spectrogram from a single bridge for a speed ramp done with the 9-vane plate in the far position, at a 'high' flow coefficient. Figure 26 shows the spectrogram from the same bridge for the same speed ramp done with the 9-vane plate in the close position. And Figure 29 shows a spectrogram for the same bridge for a 'constant flow' speed ramp done with the 27-vane plate. Spectrograms for the 27-vane boustrophedonic test data are not shown because in that testing the flow and speed change in non-linear fashions and interpreting a spectrogram vs time is not easy to do. Lastly, Figures 24, 27, 30, and 32 show the pseudo-transfer function amplitude $\hat{H}_{xy}$ for each bridge plotted against 27N frequency for all the stator plate test data.

The test results showed that there did appear to be a strain response at 27N in some but not all conditions/configurations. The 9-vane close configuration did not appear to result in a 27N forcing function on the blades, but the 9-vane far configuration and the 27-vane configuration did. The most-downstream gauge positions had the highest response at the 27N forcing function frequency, while the most-upstream locations had little to no response. Also, the spectrograms show that there was little to no forcing function response at flow coefficients around the design flow coefficient. A response was only detected at flow coefficients far off-design, at high flow coefficients above 130% of the design flow coefficient. The response only seemed to occur when the pump head rise was close to zero or negative, i.e. when it was in an overflow condition. It is hypothesized that at lower flow coefficients where the pump is producing a pressure rise the localized back flow associated with the pressure rise overcomes or washes out the incoming stator-induced pressure variation. Thus the blades do not react to the stator plate pressure field except when in an unloaded state.

If we do assume that the pseudo-transfer functions from the middle and downstream positions at high, off-design flow coefficients do indicate a resonant response, then to estimate damping from $\hat{H}_{xy}$, the following procedure can be used for each bridge considered:

1. The pseudo transfer function $\hat{H}_{xy}$ is generated as a function of time and then a 100-point moving average is applied to it, as well as the time history of 27N frequency.
2. The peak amplitude $\bar{H}_p$ of the moving average is found along with the corresponding frequency f_p.
3. The half quadratic gain level $\frac{\bar{H}_p}{\sqrt{2}}$ is calculated and the closest frequencies above and below f_p with amplitudes that are equal to or less than $\frac{\bar{H}_p}{\sqrt{2}}$ are found.
4. Those frequencies are denoted f_l, and f_u, and along with f_p can then be used in the half quadratic gain equation to estimate the critical damping ratio.

The tracking data were made with a block size of 8192 points, which at a 20480 Hz sample rate gives estimates over 0.4 second blocks. Therefore a 100 point moving average is like averaging over a 40 second window. The RPM dwells in these speed ramps were usually 30-40 seconds long, so this long averaging process acts over approximately the duration of a single speed dwell.

For the 27-vane stator boustrophedonic test series a moving average was not applied, since both flow rate and speed were swept as a function of time. Instead, the average amplitude of $\hat{H}_{xy}$ was calculated over discrete flow/speed intervals and damping was estimated in a similar manner as described above.

Table 10 shows some frequency and damping estimates taken from the 9 and 27-vane stator test data.

Table 10: Damping ratio and peak frequency from stator plate testing. Values are the average values from the high flow stator plate conditions, over Bridges 3, 6, and 9

Configuration -	f_p Hz	ζ -
9 vane far	1703	0.078
27 vane constant flow	1600	0.055
27 vane boustrophedonic	1551	0.055

SUMMARY

The results of the stator plate testing are not as voluminous as the ping test results, but both methods may offer insight into the damping of spinning blades. The stator testing seemed to excite modes in the 1.5-1.7 kHz range. The ping test results showed relatively large responses in the 2.2 kHz frequency range, but also showed responses in this lower frequency range. The damping results from this lower frequency range were on average around 3% critical damping. The damping estimated from the stator test ranged from 5.5% to 7.8%, which is higher than the either the average damping from the ping testing in the 1.6 kHz and 2.2 kHz range, but is within the 2.2 kHz 95% confidence intervals from the ping testing. Also the ping data did tend to show a positive correlation of damping with amplitude, and the 1.6 kHz range responses were on average smaller amplitude than the 2.2 kHz responses. For the modes in the 2.2 kHz range, the ping testing average weighted damping was 4-5% critical damping.

Also, the ping testing results showed a relatively wide distribution in damping ratio estimation. The damping extraction process estimated damping over 10% in some pings, and less than 1% for others at the same operating conditions. While a significant effort was made to exclude data of poor quality, the low strain amplitudes and ping excitation method certainly provided a challenging data set to work with. Moreover, it should be noted that the strain gauge bonding and waterproofing likely had an effect on the blade natural frequencies and damping that would not be present in an un-instrumented blade. The exact degree to which these factors affect damping was not quantified, but it is likely that the as-tested configuration would show more damping than a blade with no gauges installed.

One result worth noting is that the ping data seemed to show, for presumably similar modes, on average, damping in air is lower than damping in quiescent water, which is in turn lower than damping in water while spinning. There was too much variation in the damping results to correlate the spinning damping data to shaft speed, flow rate, or inlet pressure, but the data did show that damping does appear to be affected by spinning the inducer.

The force input for the stator testing was intended to be a discrete forcing function at 27N with a 27θ spatial shape. The ping input was intended to be an impulsive base excitation. The different nature of excitation and the efficacy with which each forcing function was transmitted to the blades likely affected what modes tended to get excited, which may explain why the ping test showed responses at 2.2 kHz and the stator testing did not.

Both the stator and ping testing results were challenged by issues with the force input. Ideally, a measured forcing function would be applied directly to the blades. In either case, this was not fully achieved. These limitations should be considered when interpreting the damping results from this test series.

Overall, the ping test and stator test results showed that on average, the subscale inducer blades at realistic operating conditions in water experienced critical damping ratios in the 4-7% range, and moreover that the critical damping ratio may be weakly proportional to the amplitude of the blade motion.

FORWARD WORK

The ultimate goal of this effort is to determine appropriate damping values to apply to full scale hardware in actual flight conditions. The results from this test may indicate some damping trends to expect. For example, the test indicates that damping ratios measured on a spinning inducer are on average higher than damping ratios measured during quiescent conditions. Hydrodynamic forces tend to scale with the inducer tip dynamic pressure (which accounts both for scale, density, and speed), but it still remains to identify appropriate scaling laws to infer damping ratios from one geometry scale to another, and one working fluid to another. The amount of influence of fluid on the structure or the propensity for the fluid acoustics to couple with the structural dynamics must also be considered when attempting to estimate a realistic amount of damping on a given structure. This is certainly not a straight-forward effort and is not addressed in this paper, rather, it is left for future work.

ACKNOWLEDGEMENTS

This work was funded by the Space Launch System Liquid Engine Office at Marshall Space Flight Center.

References

[1] Peng, Levine, Shido, Leland *Experimental Observations on Material Damping at Cyrogenic Temperatures* Jet Propulsion Laboratory, 4800 Oak Grove Drive, Pasadena CA 91109

[2] Kaminer, A.A., and N. Ya. Nastenko., *Experimental investigation of hydrodynamic damping during bending oscillations of blade profiles in water flow.* Strength of Materials, 1976: 25-27.

[3] Roth, Calmon, Farhat, Meunch, Huebner, and Avellan *Hydrodynamic Damping Identification from an Impulse Response of a Vibrating Blade* 3rd IAHR International Meeting of the Workgroup on Cavitation and Dynamic Problems in Hydraulic Machinery and Systems, October 14-16, 2009, Brno, Czech Republic.

[4] B. Sontag *RS-25 Subscale Inducer Modal Test Report* SLS-DEV-17-017 Memo ET40(17-036), September 2017

[5] M.J. Casiano, *Extracting Damping Ratio From Dynamic Data and Numerical Solutions*, NASA TM 2016-218227, September 2016

FIGURES

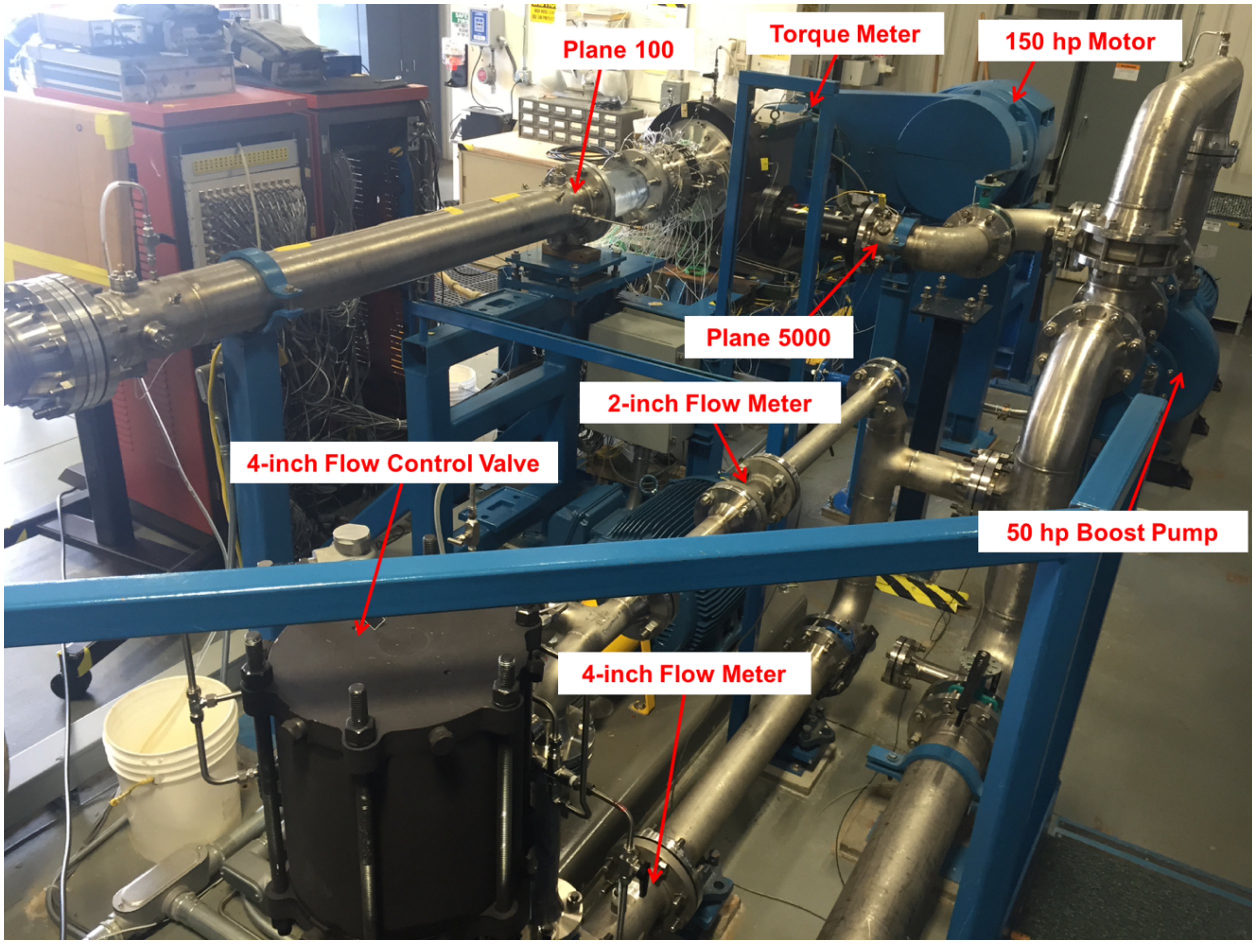

Figure 1

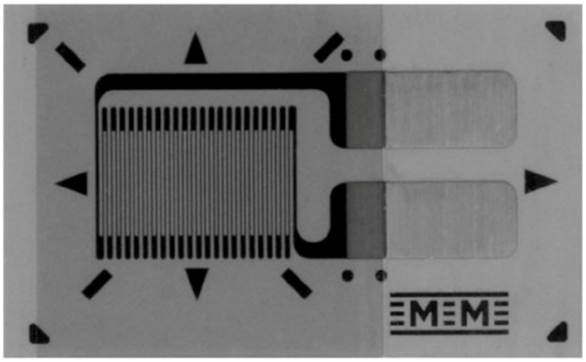

Figure 2: Vishay Micro-Measurements CEA-06-062UB-350 strain gauge

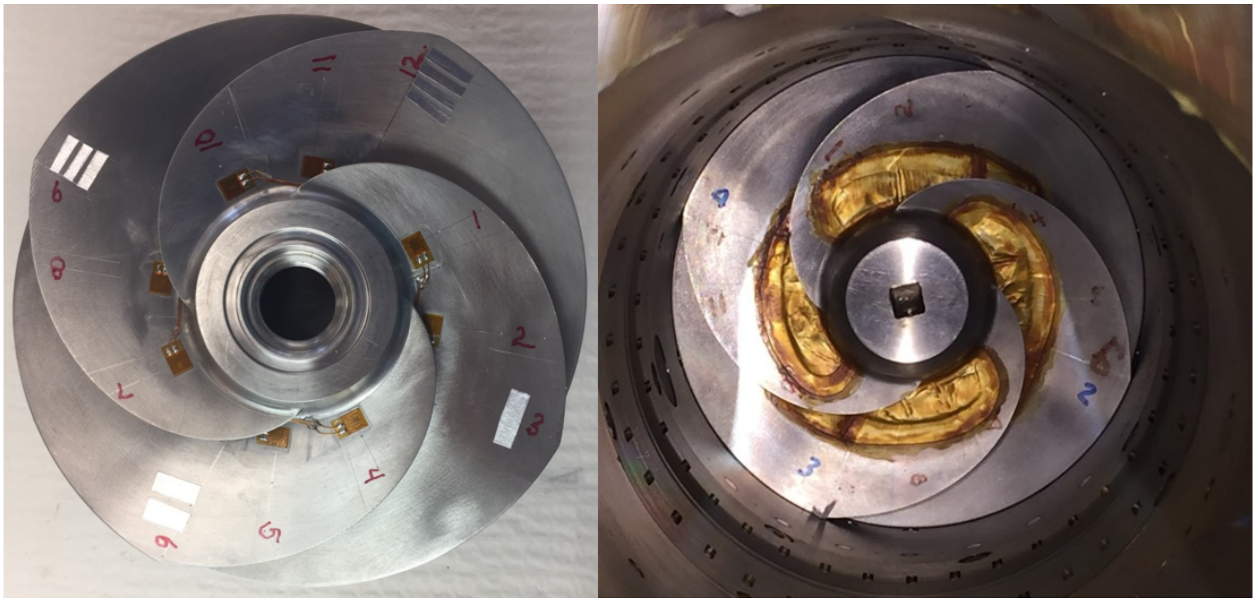

Figure 3: Inducer with strain gauges (left) and as tested with waterproofing and metal foil covers (right)

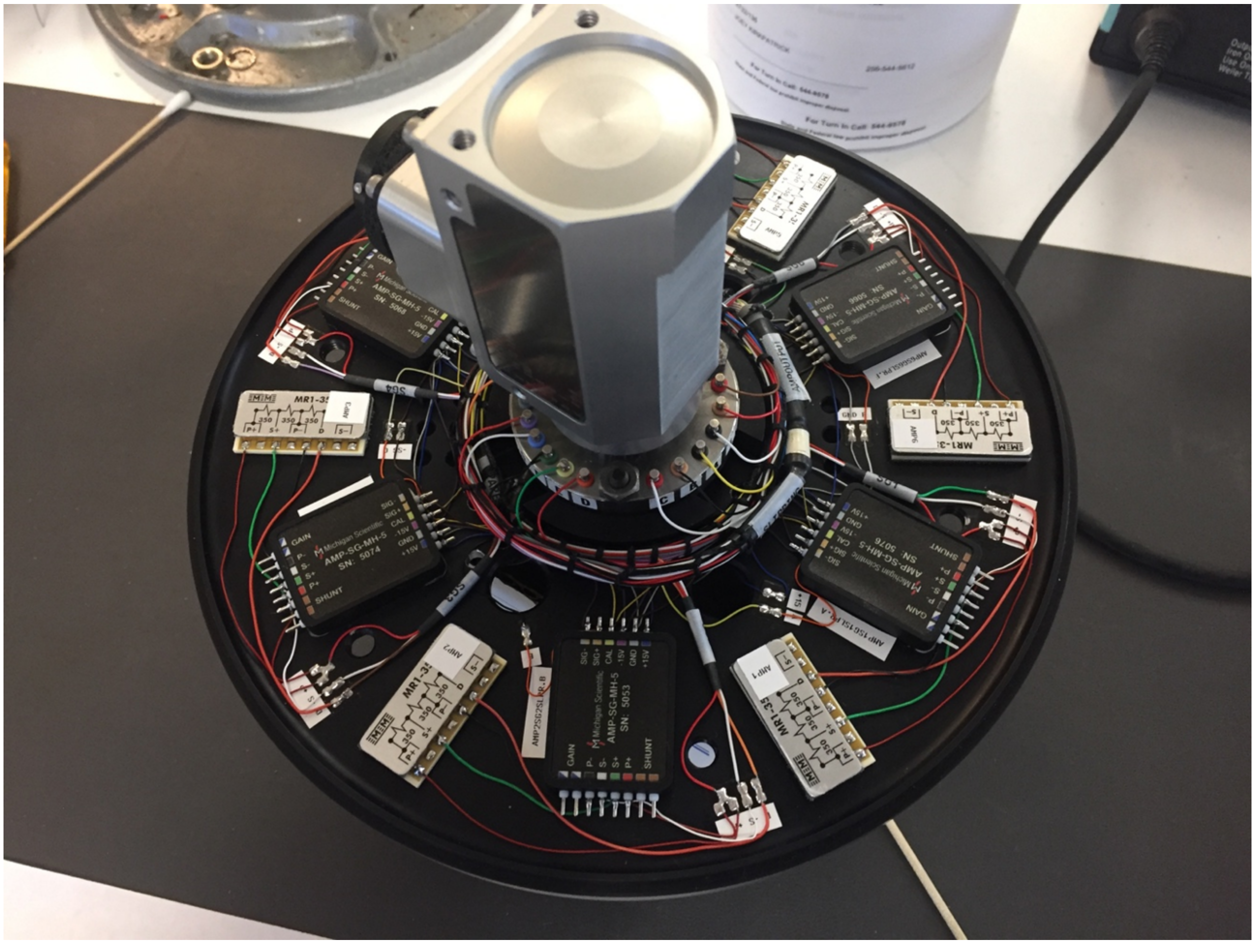

Figure 4: Wheatstone bridge/amplifier/slip ring assembly

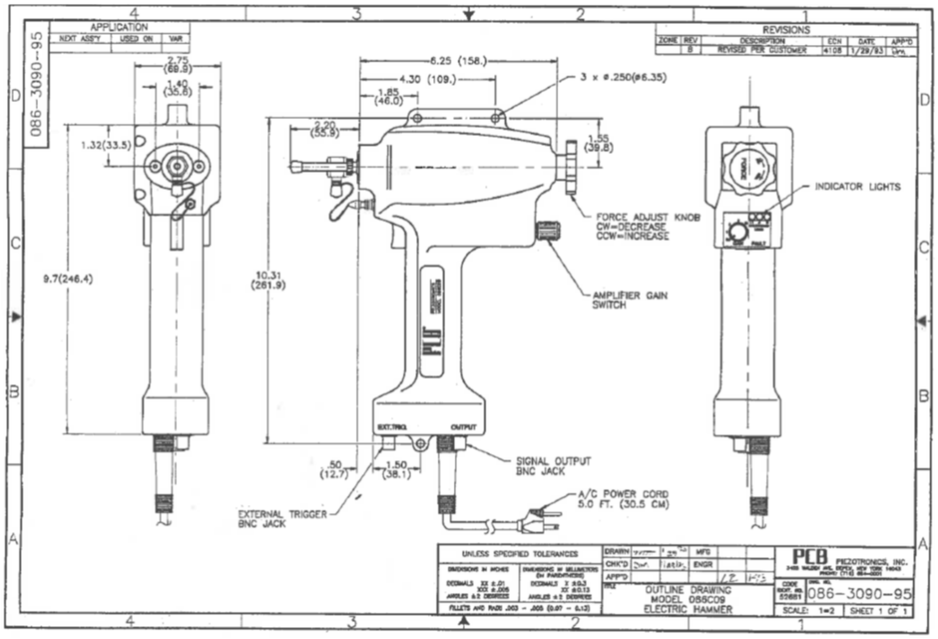

Figure 5: PCB electric hammer drawing

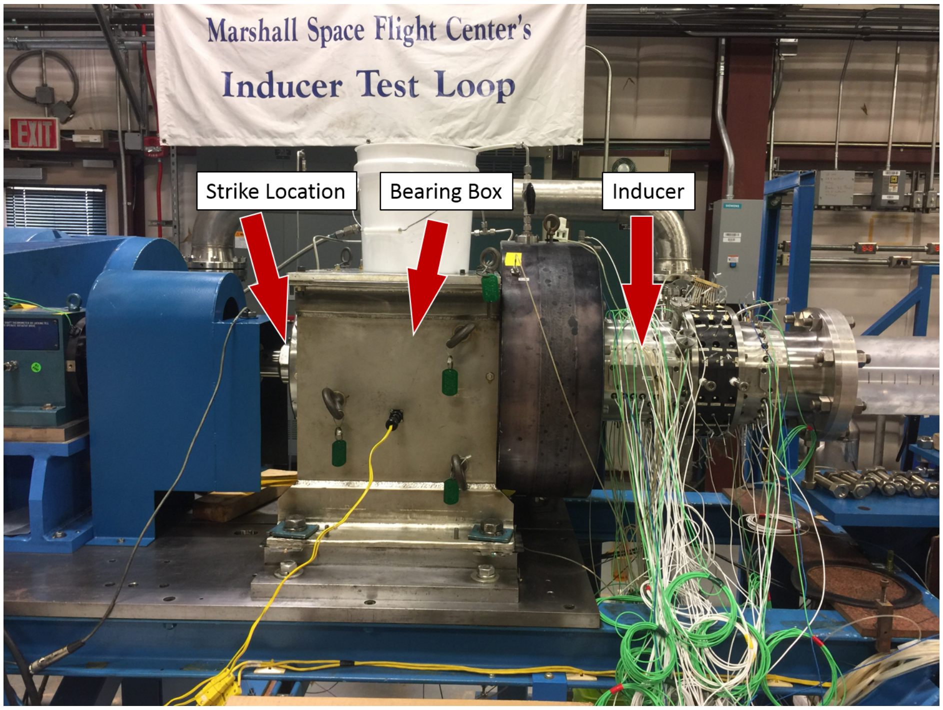

Figure 6: Ping location on the test rig

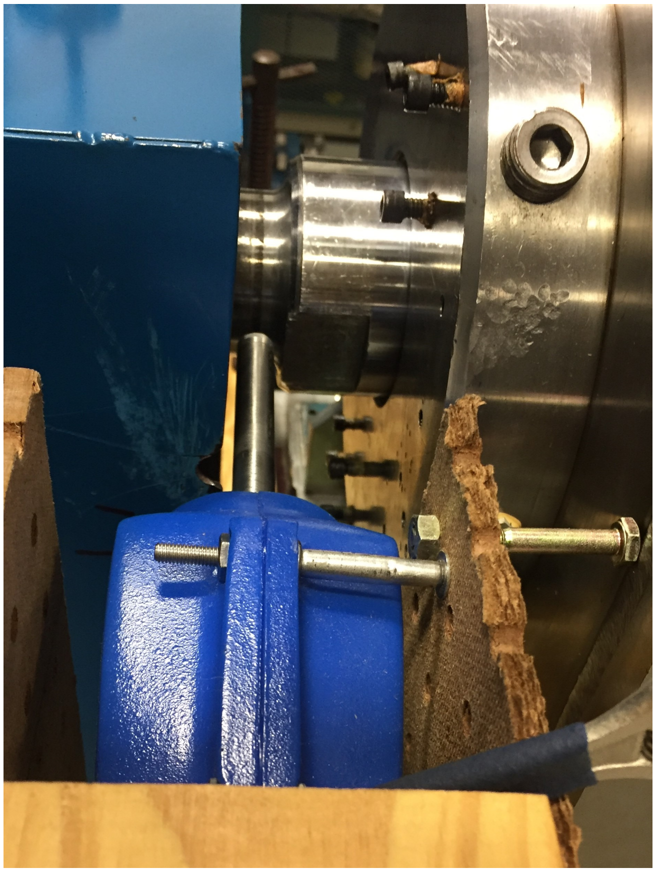

Figure 7: PCB electric hammer in position

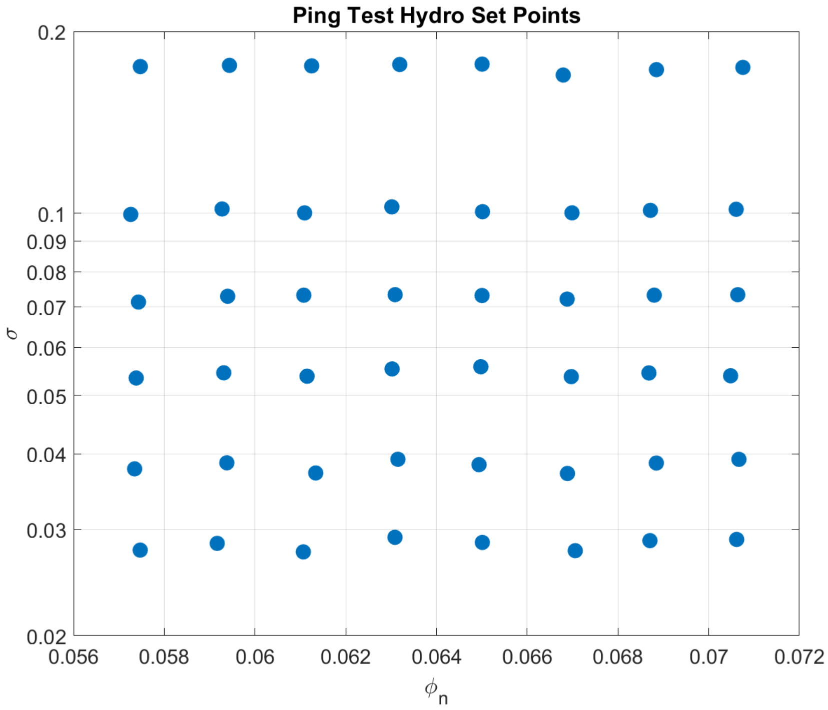

Figure 8: Ping test normalized flow coefficient ϕ_n and cavitation number σ set points

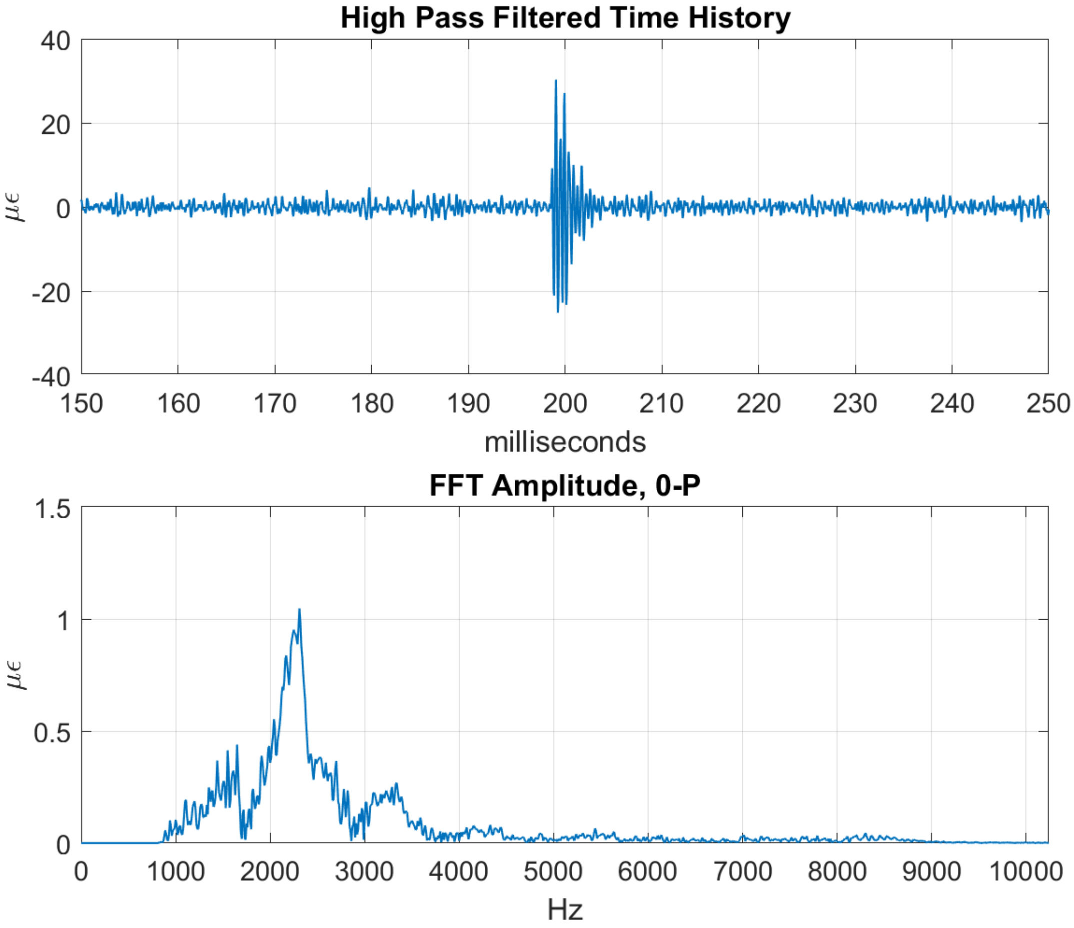

Figure 9: Example high pass filter ping response and corresponding discrete Fourier transform

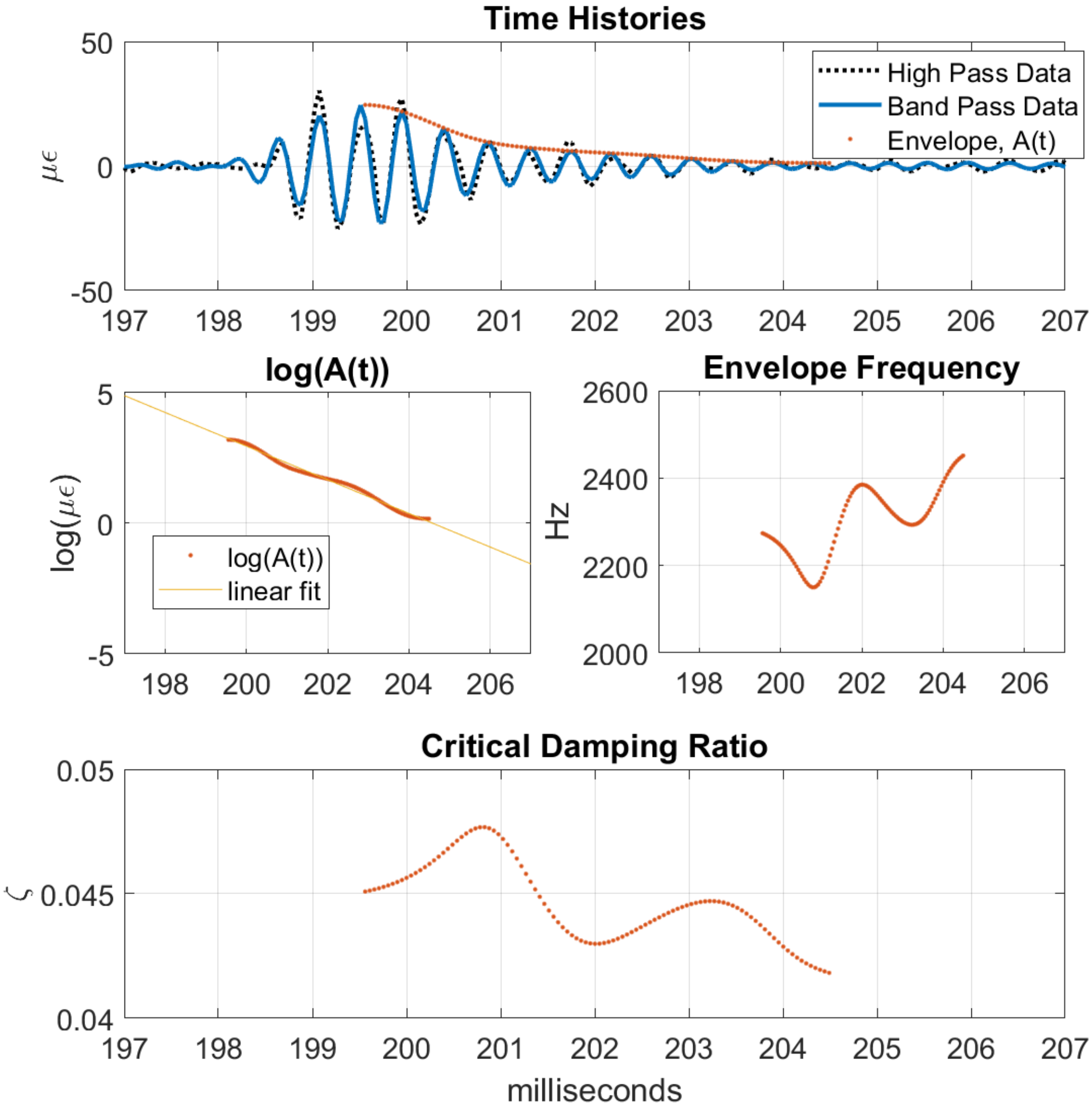

Figure 10: Example damping calculation process

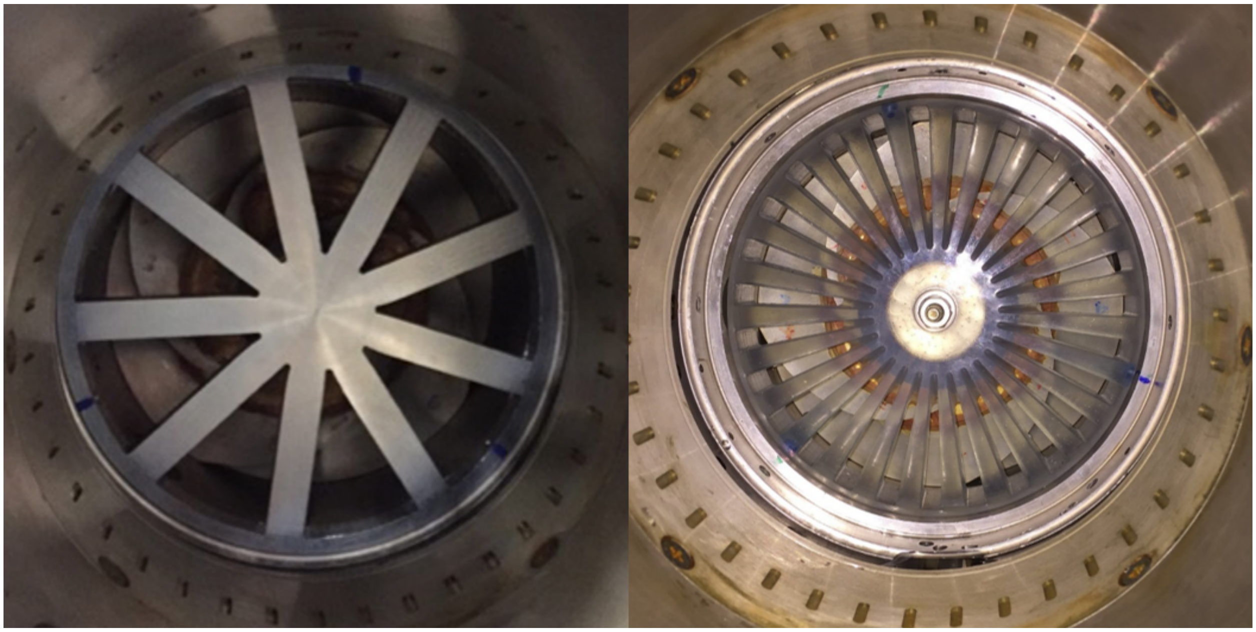

Figure 11: 9 (left) and 27 (right) vaned stator plates installed in the Inducer Test Loop

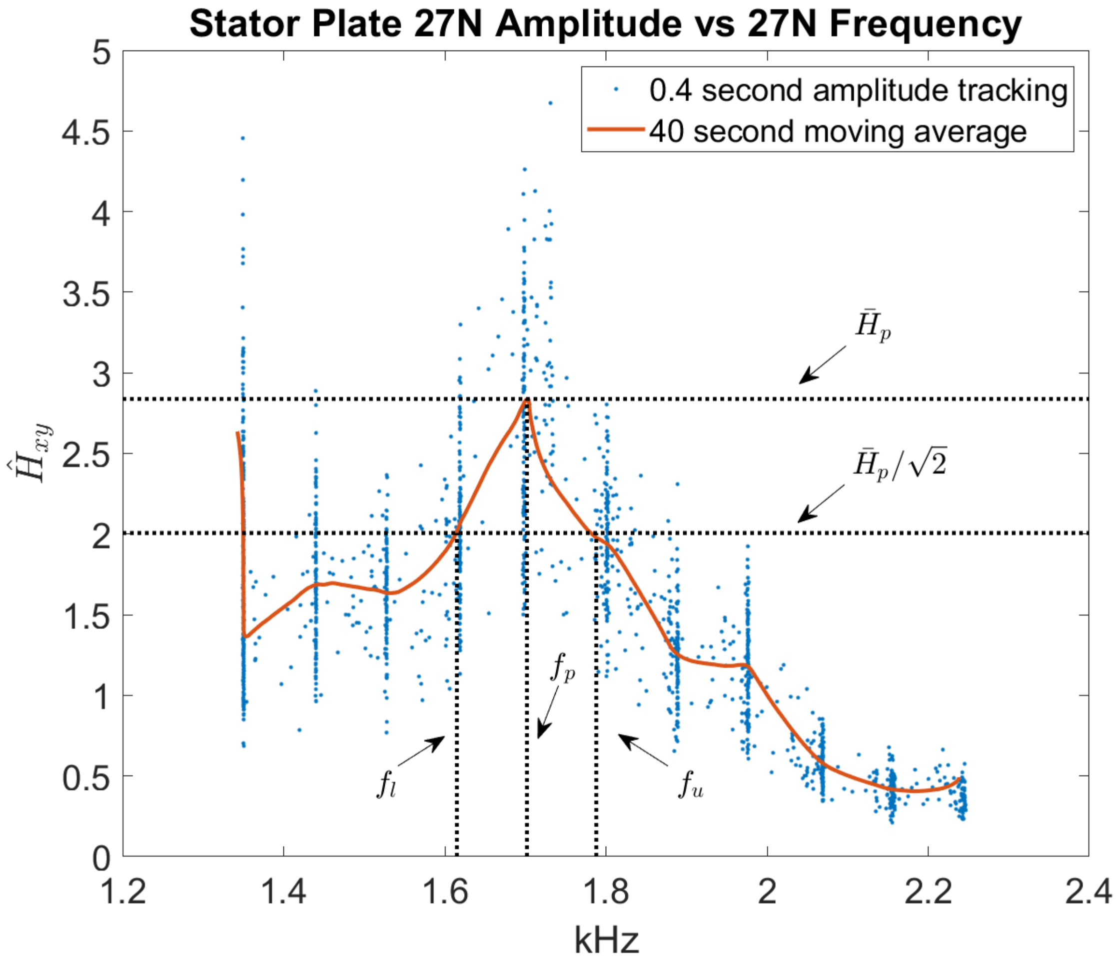

Figure 12: Example stator damping calculation process

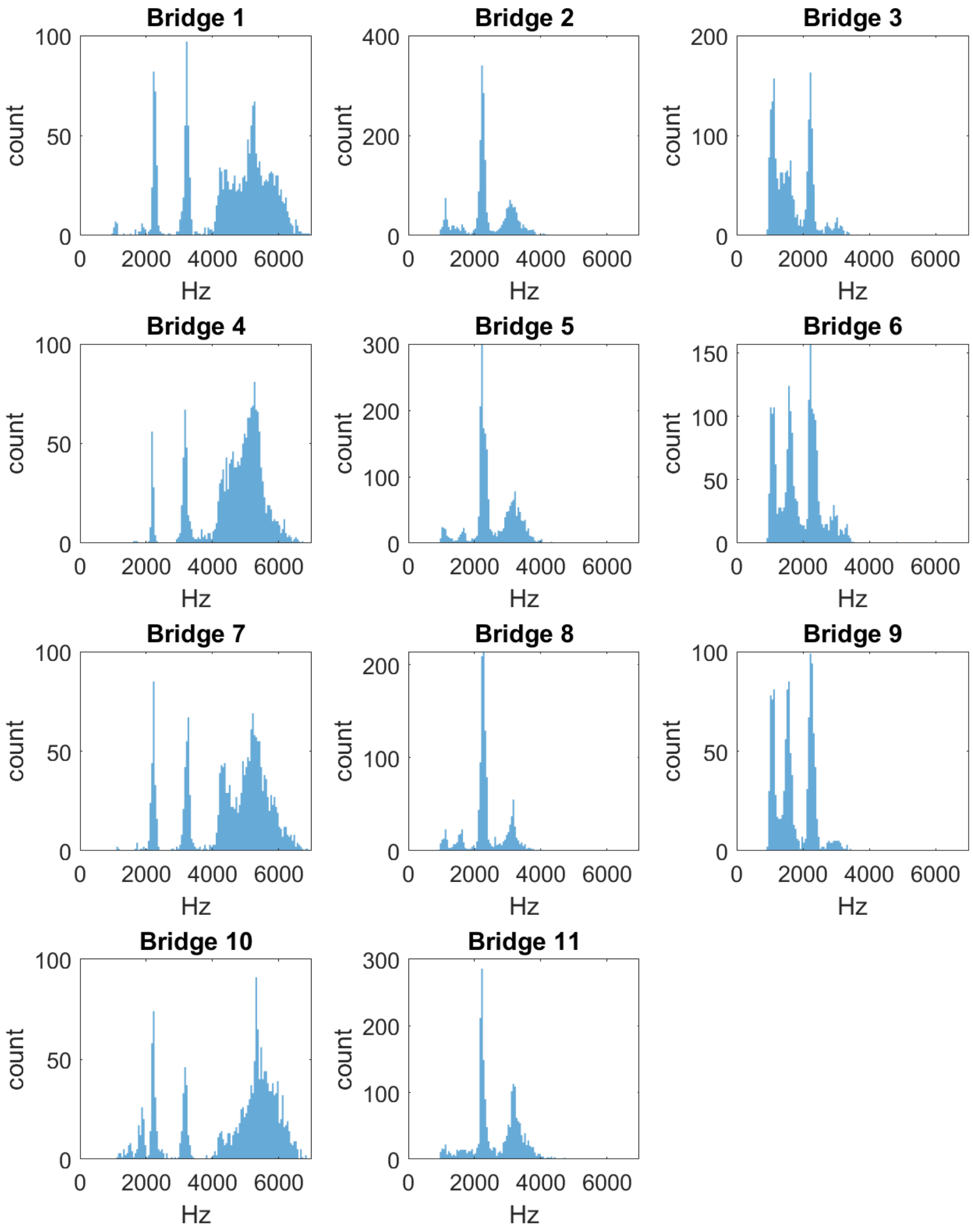

Figure 13: Ping frequency histogram for all 4200 RPM data

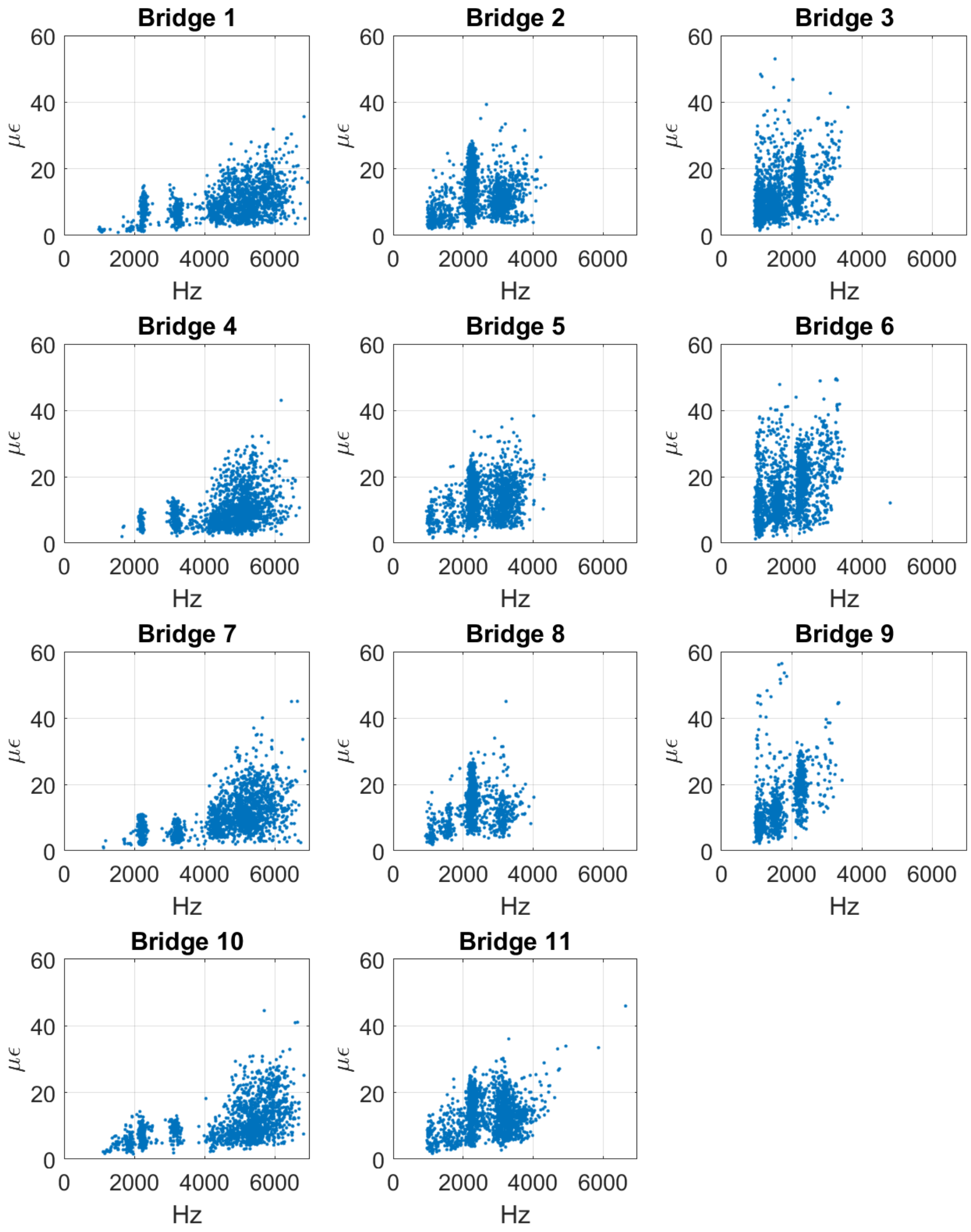

Figure 14: Envelope peak amplitude vs frequency for all 4200 RPM data

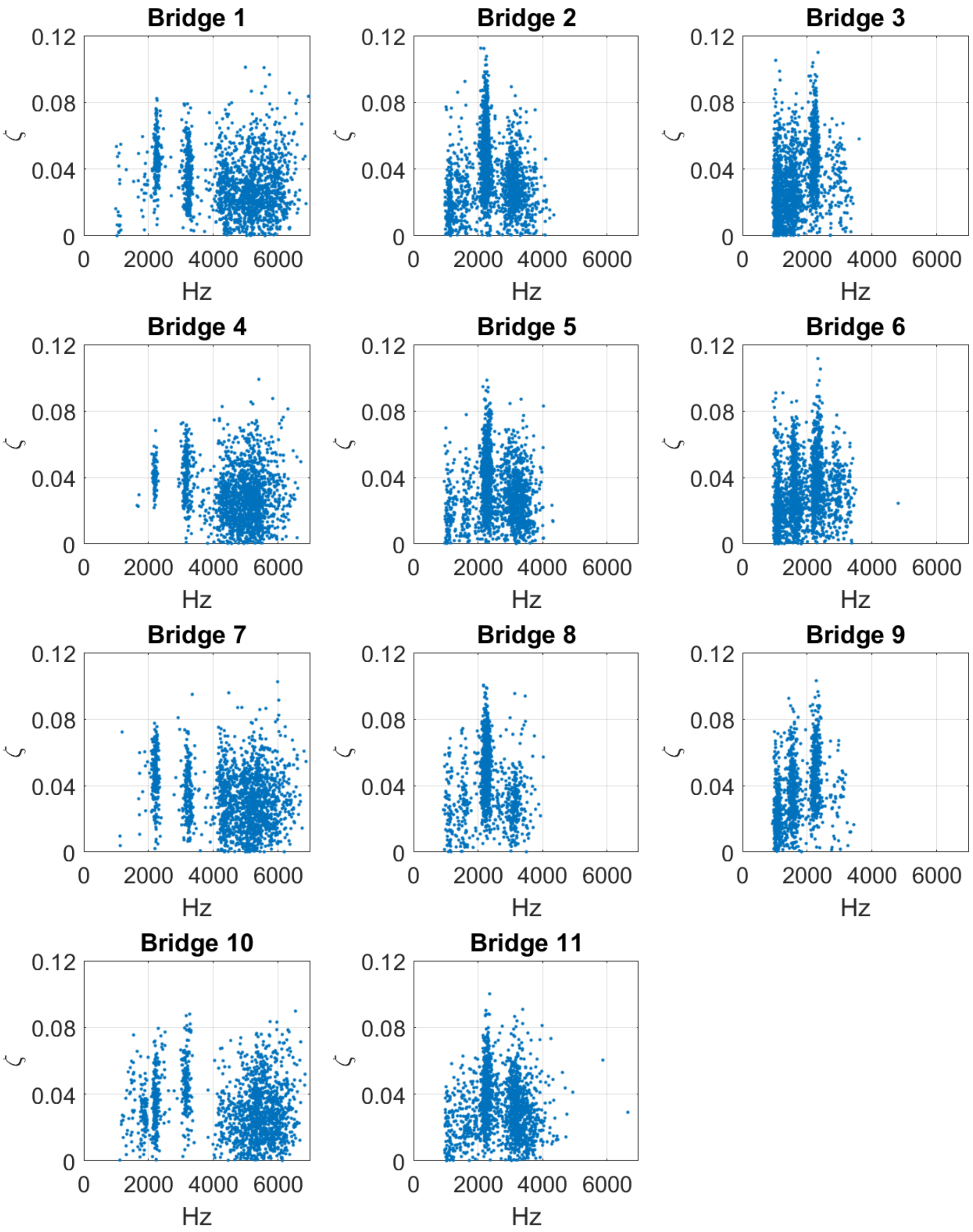

Figure 15: Critical damping ratio vs frequency for all 4200 RPM data

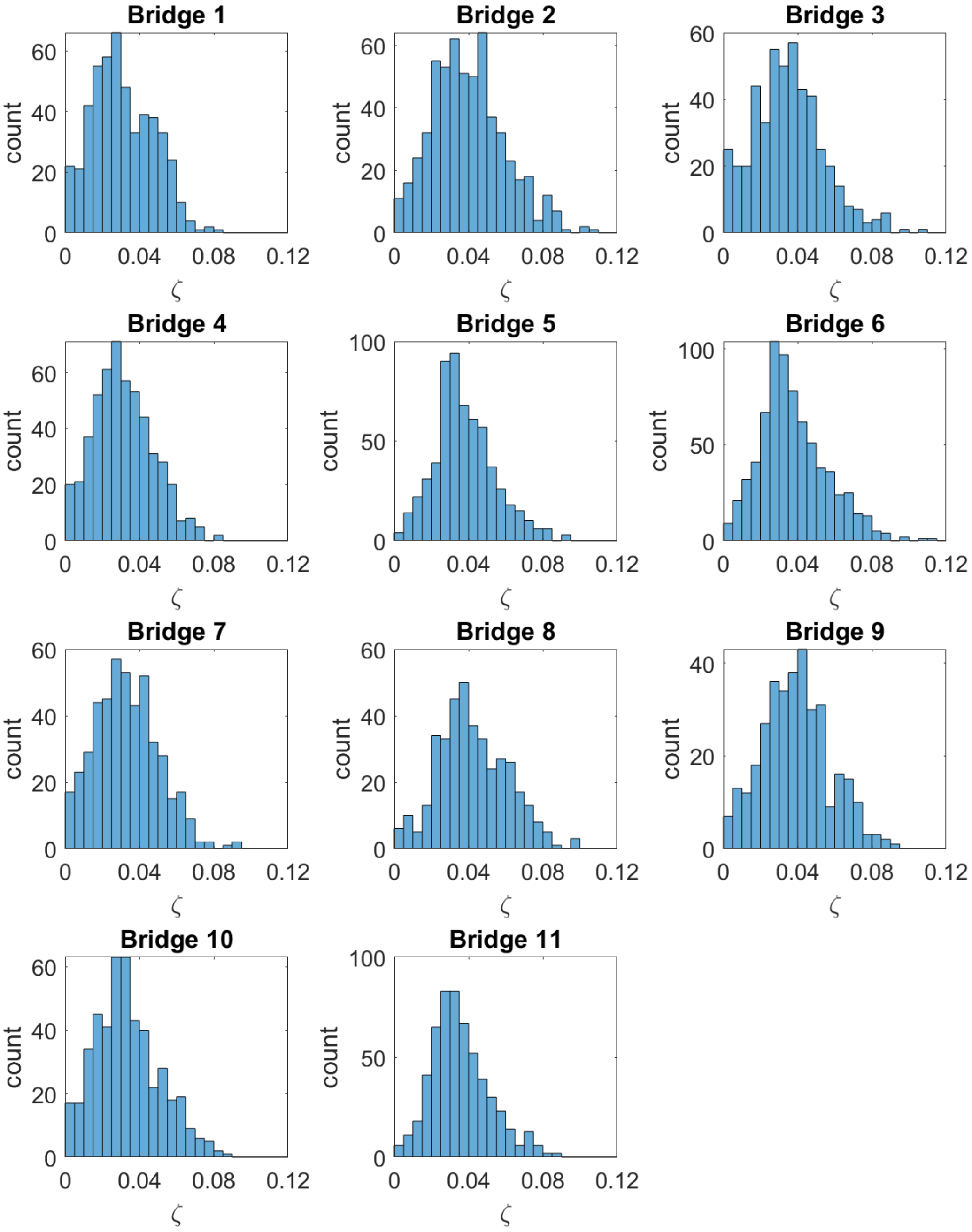

Figure 16: Critical damping ratio histogram for frequencies between 2 and 2.5 kHz, at 4200 RPM

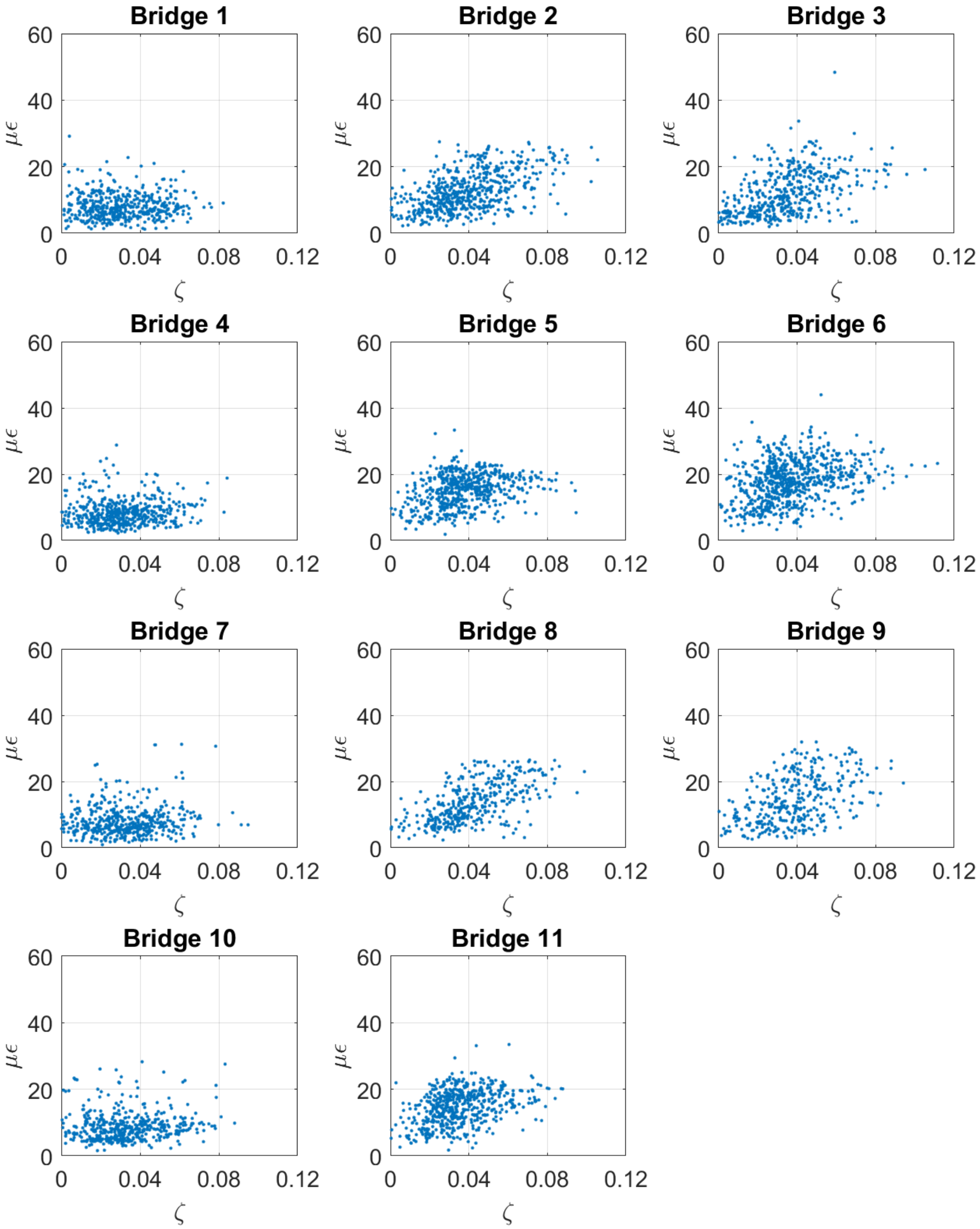

Figure 17: Envelope peak amplitude vs estimated damping for frequencies between 2 and 2.5 kHz, at 4200 RPM

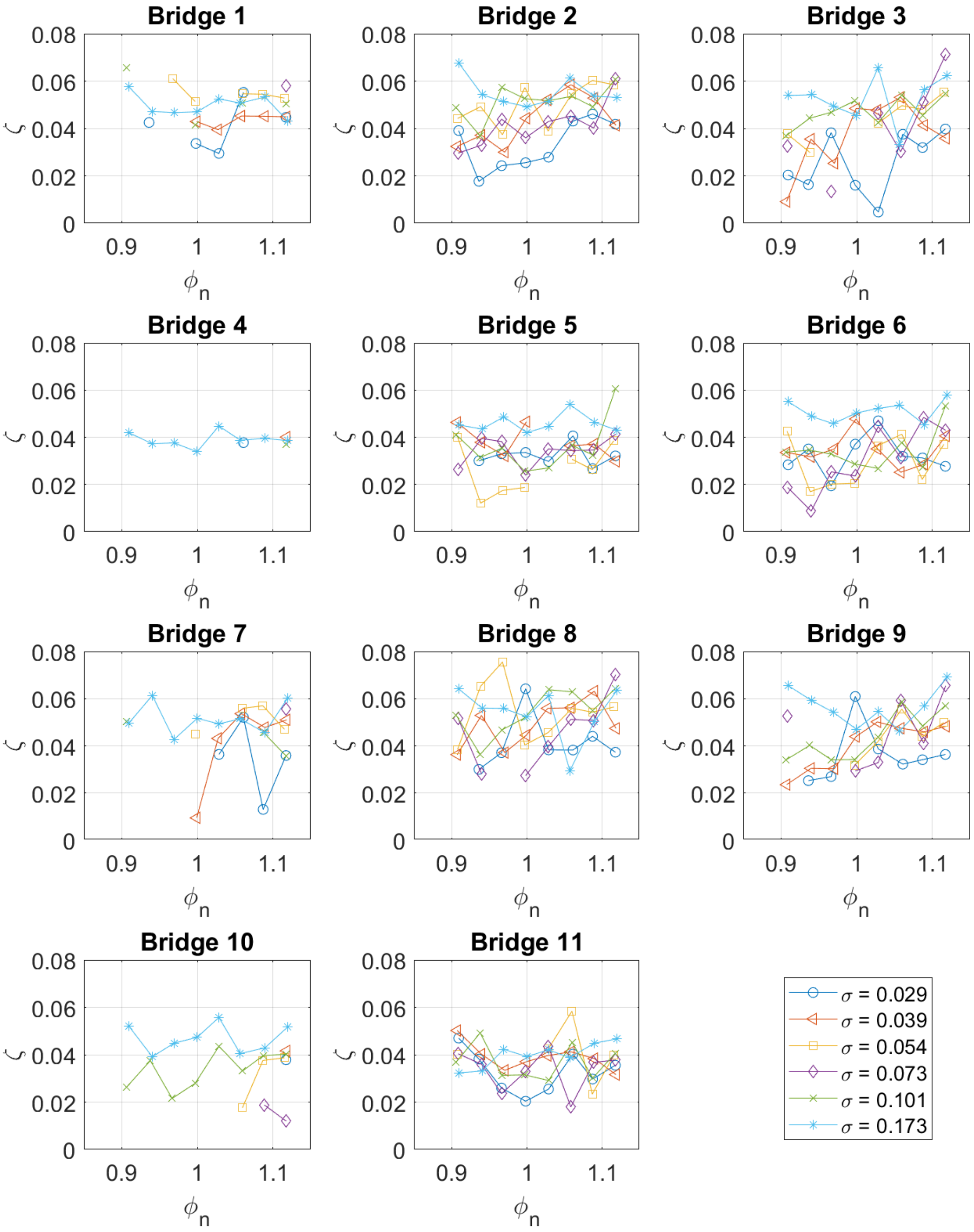

Figure 18: Weighted average damping ratio vs flow coefficient for frequencies between 2 and 2.5 kHz, at 4200 RPM

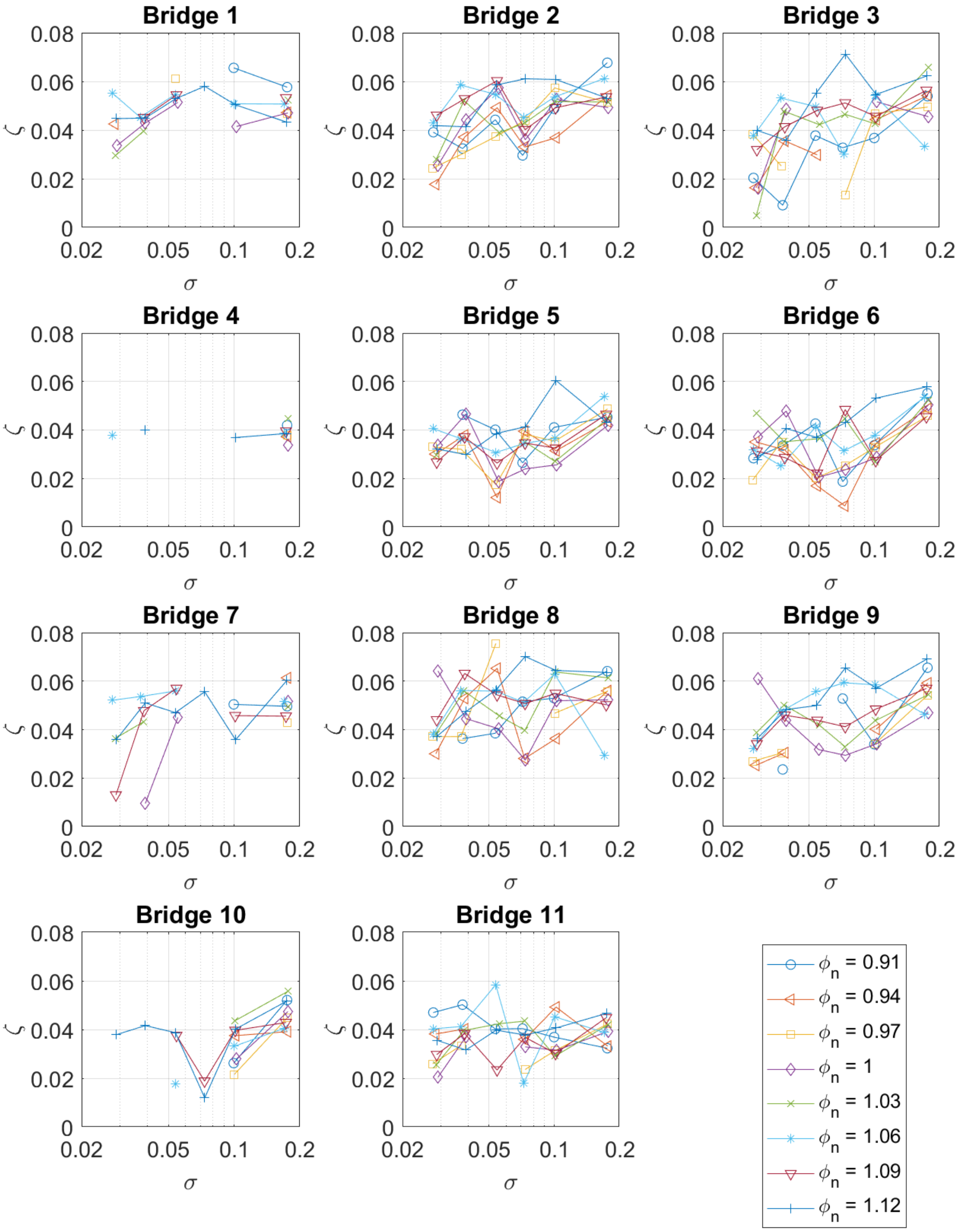

Figure 19: Weighted average damping ratio vs cavitation number for frequencies between 2 and 2.5 kHz, at 4200 RPM

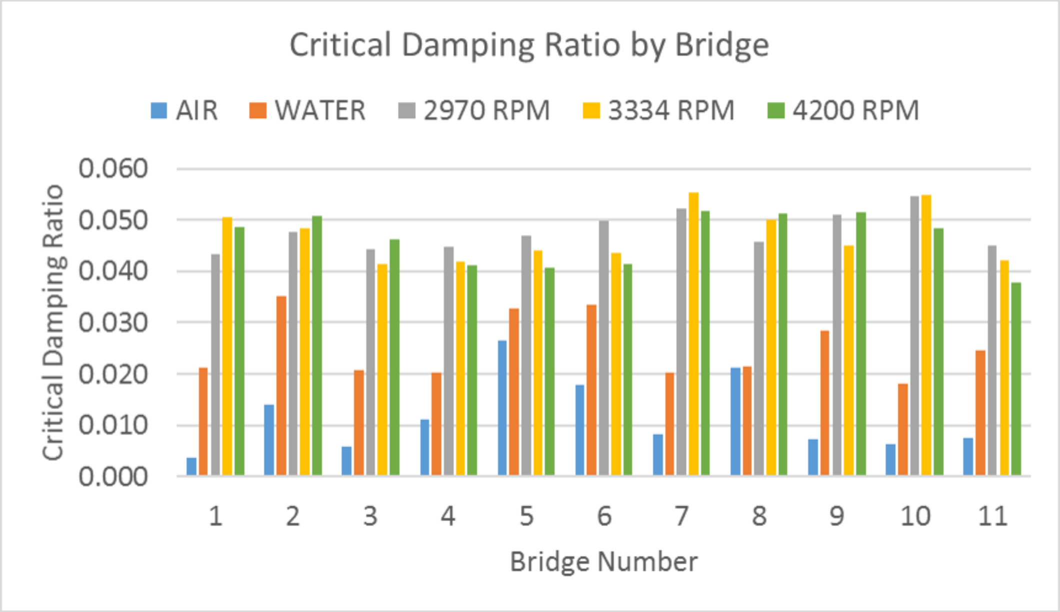

Figure 20: Average σ_r-based damping ratio over all conditions (3-4 kHz for air, 2-2.5 kHz for water)

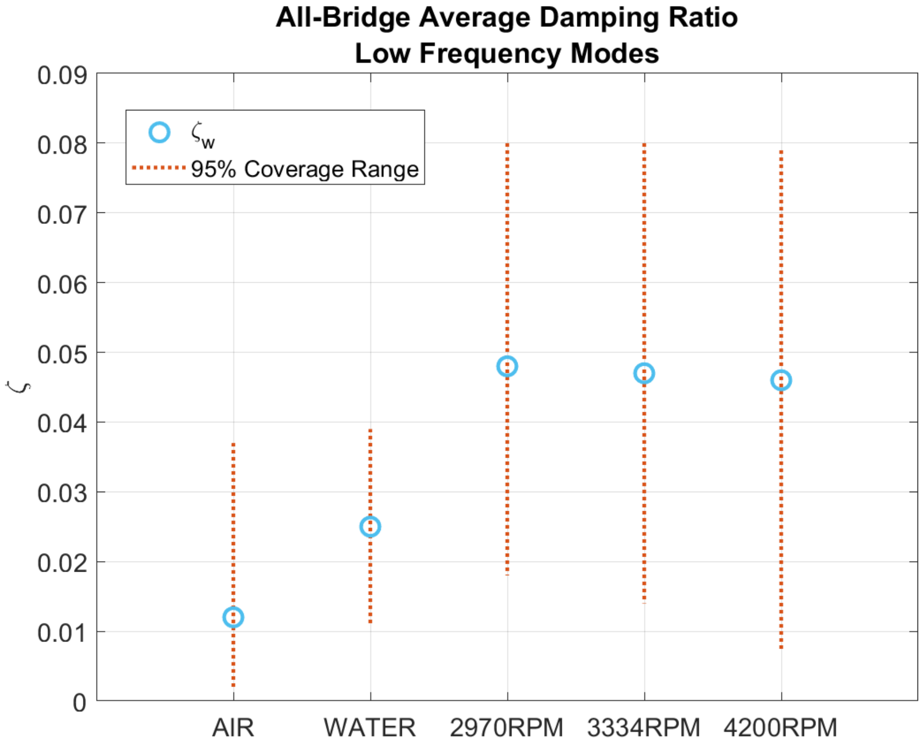

Figure 21: Average σ_r-based damping ratio over all conditions and bridges (3-4 kHz for air, 2-2.5 kHz for water)

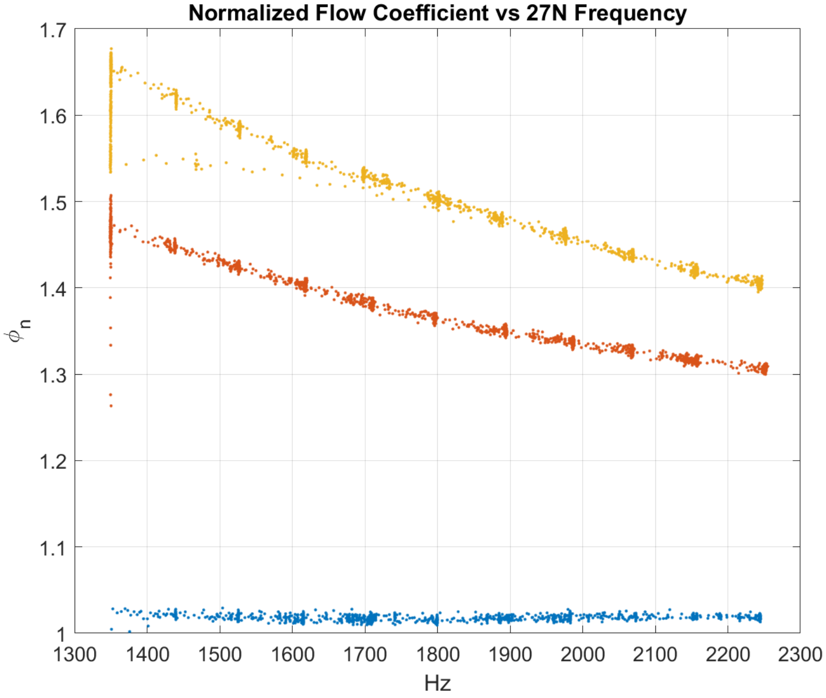

Figure 22: Normalized flow coefficient vs 27N frequency, 9-vane ‘far’ configuration

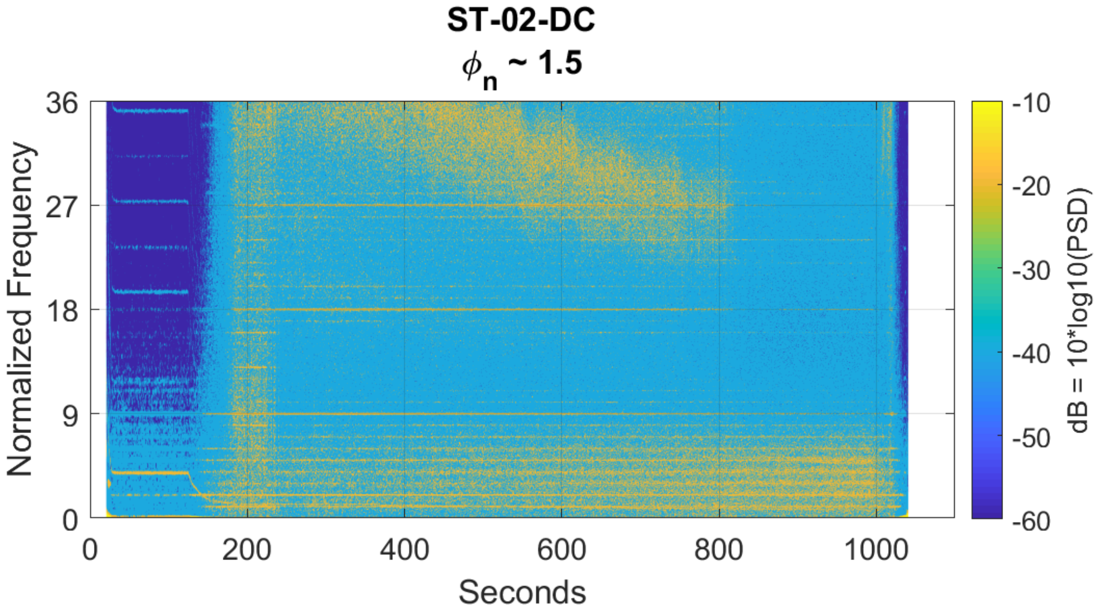

Figure 23: 9-vane speed ramp spectrogram from bridge 2, $\phi_n \sim 1.5$, ‘far’ configuration

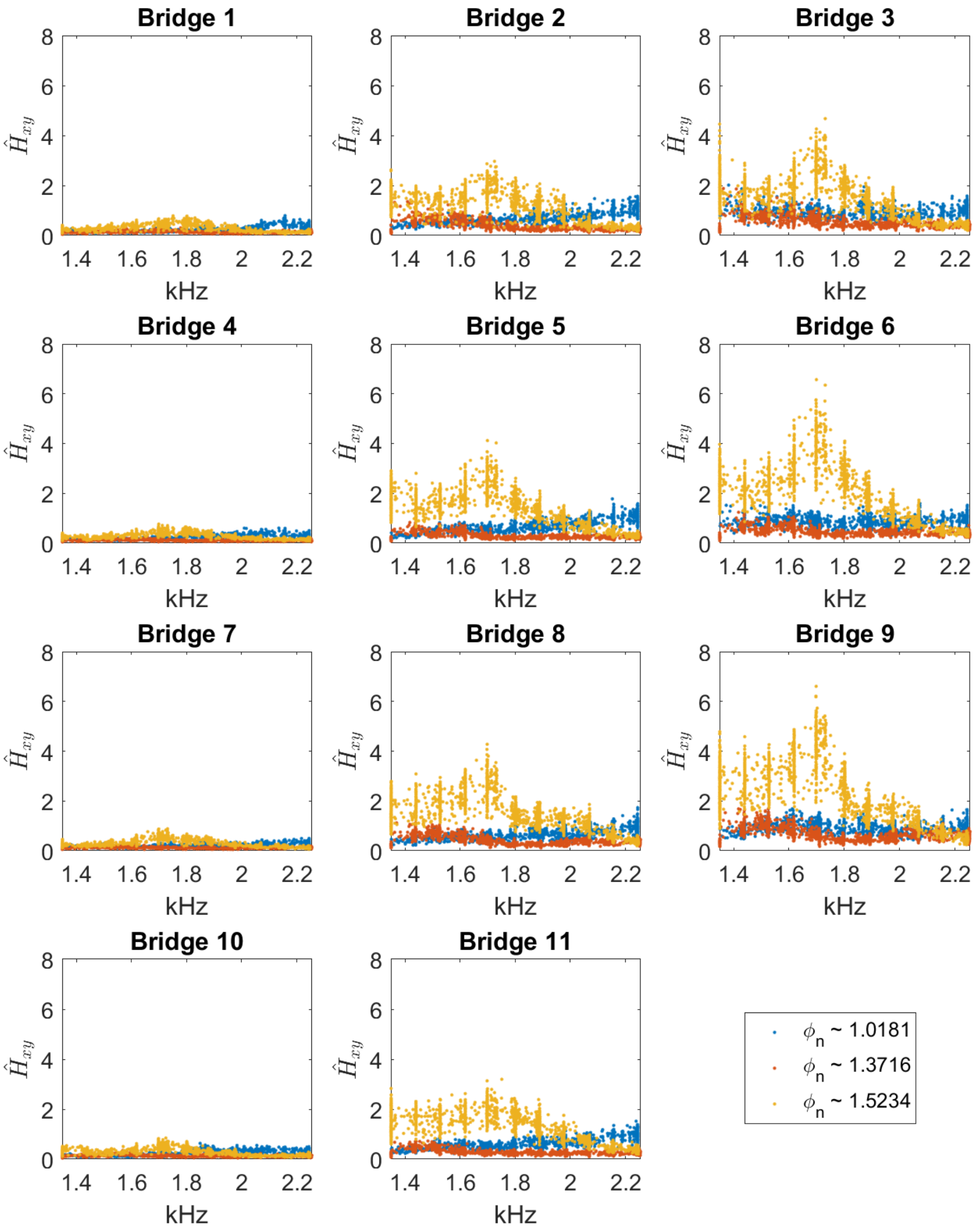

Figure 24: Psuedo-transfer function amplitude vs 27N frequency, 9-vane ‘far’ configuration

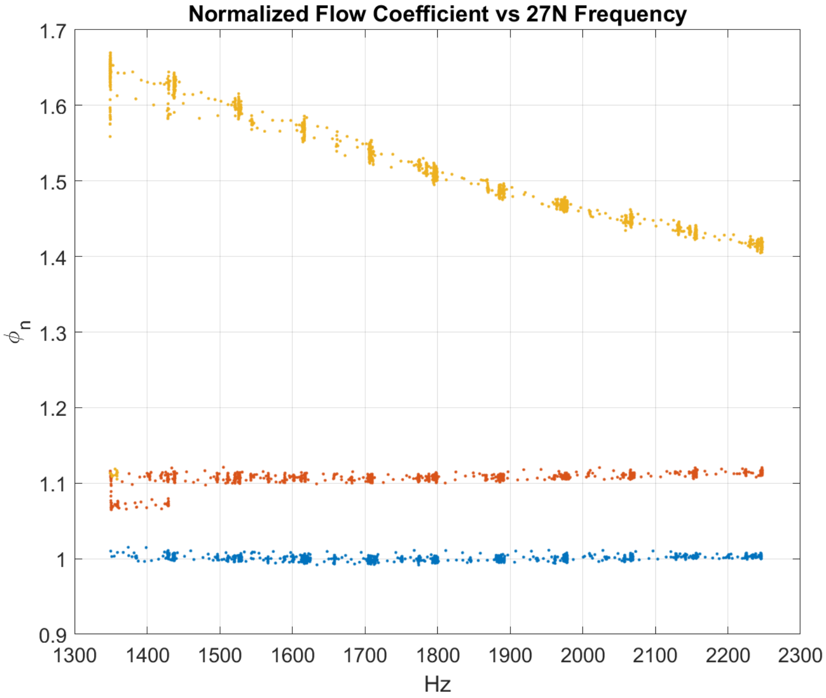

Figure 25: Normalized flow coefficient vs 27N frequency, 9-vane 'close' configuration

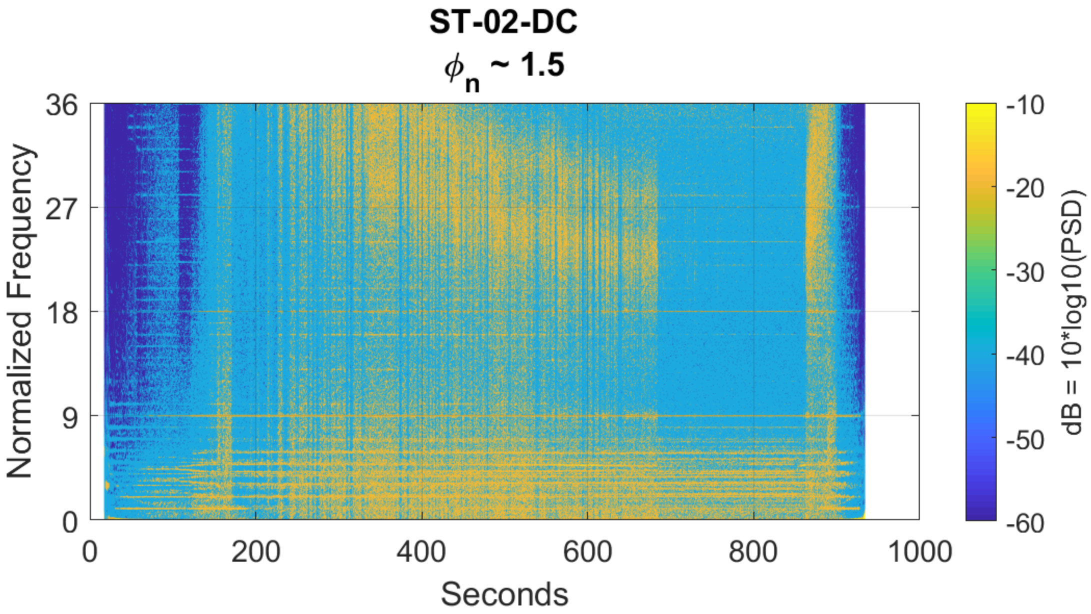

Figure 26: 9-vane speed ramp spectrogram from bridge 2, $\phi_n \sim 1.5$, 'close' configuration

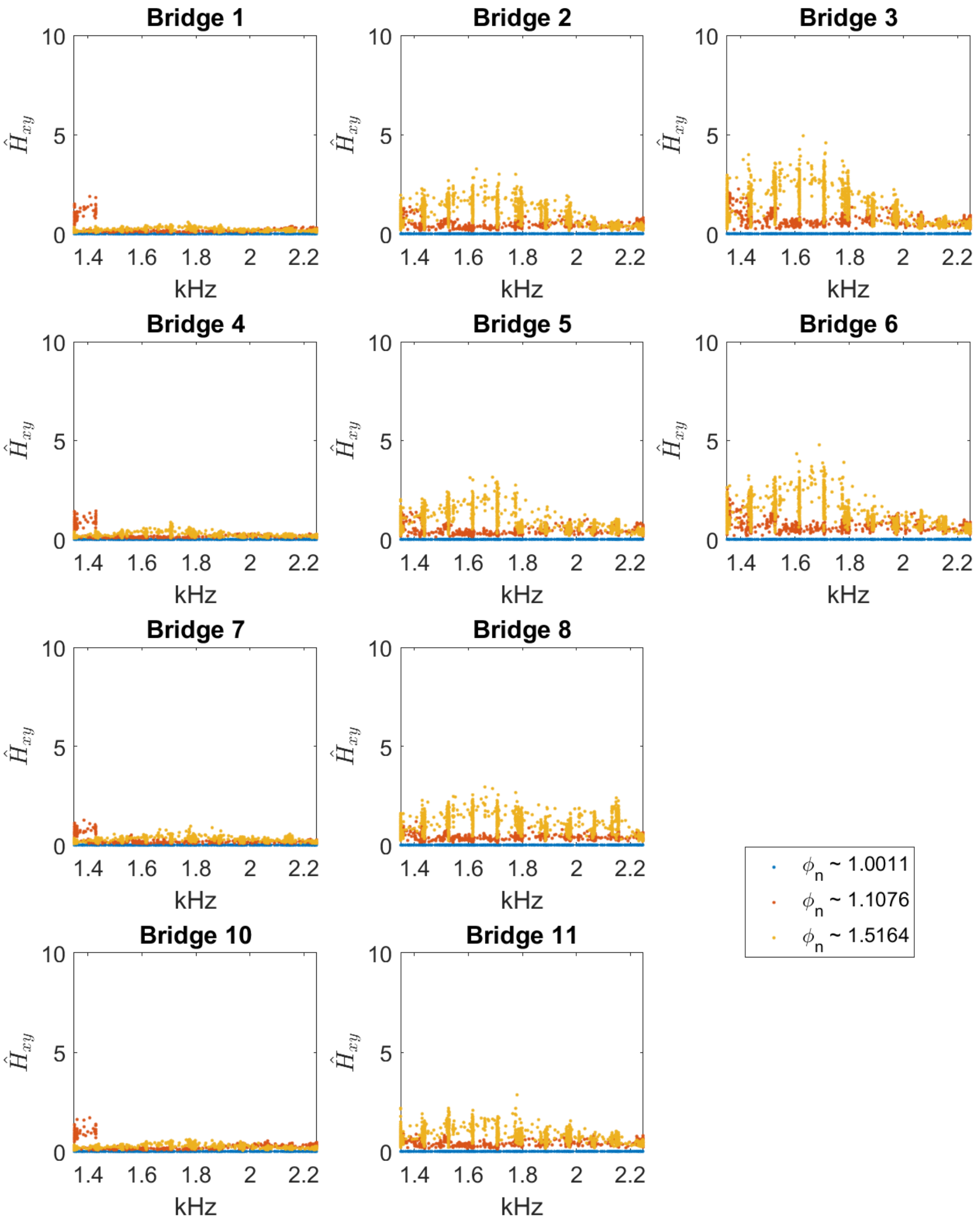

Figure 27: Psuedo-transfer function amplitude vs 27N frequency, 9-vane ‘close’ configuration

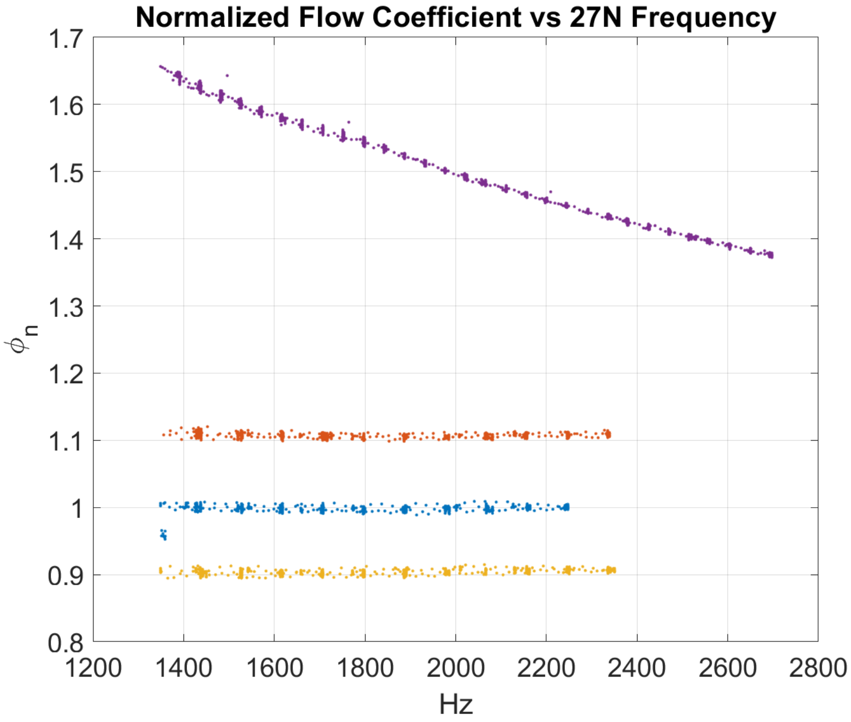

Figure 28: Normalized flow coefficient vs 27N frequency, 27-vane configuration

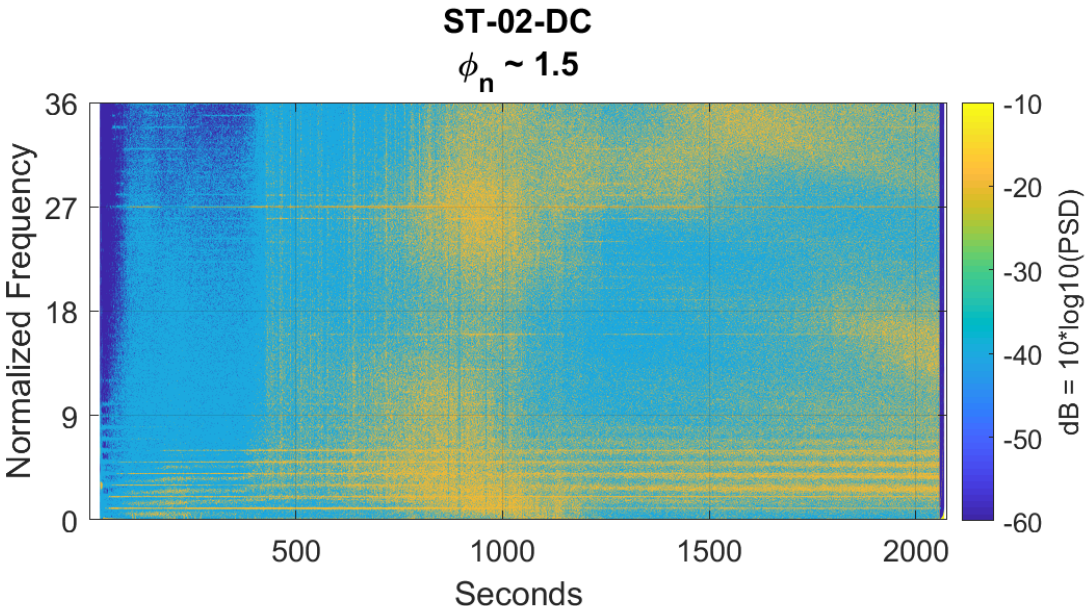

Figure 29: 27-vane speed ramp spectrogram from bridge 2, $\phi_n \sim 1.5$

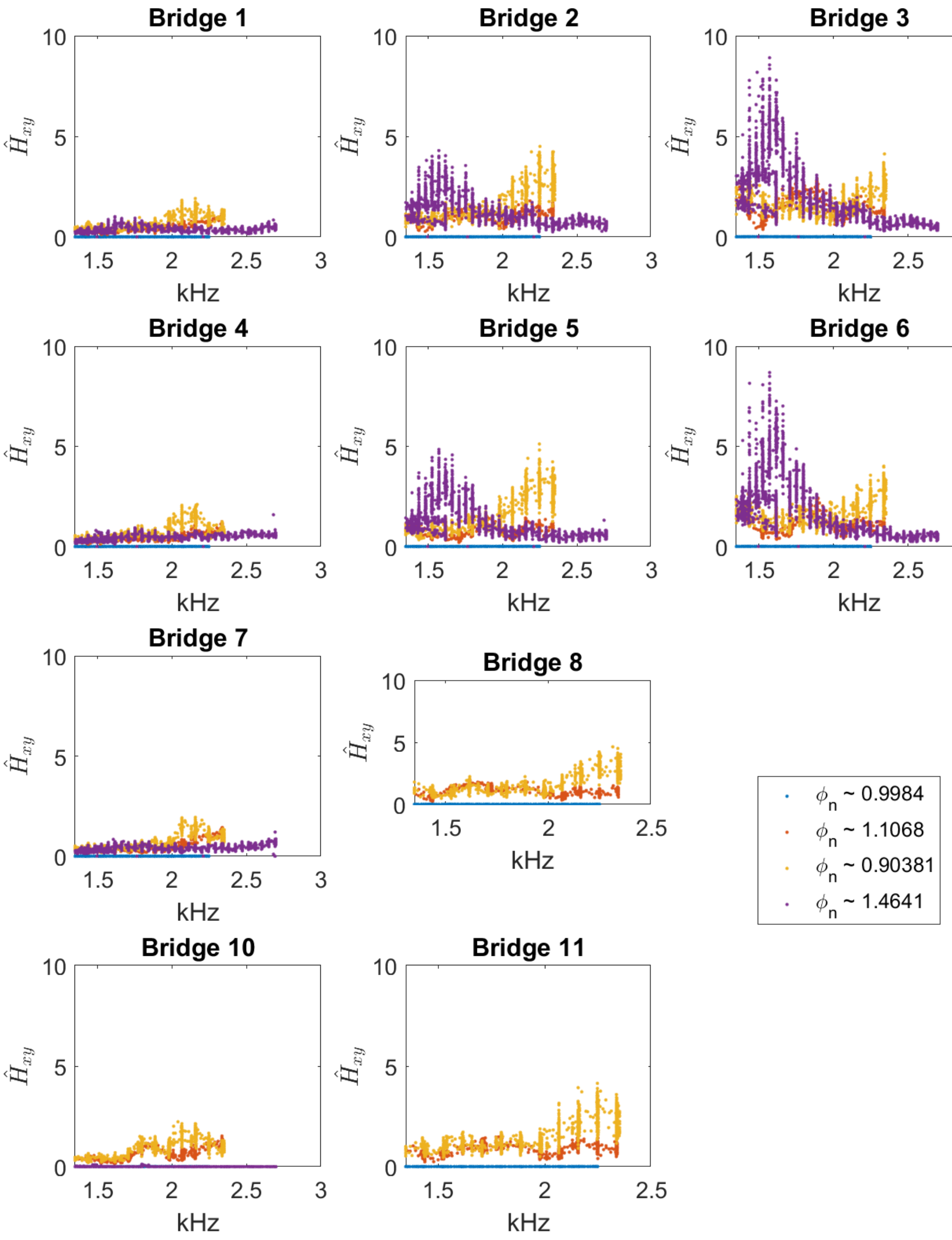

Figure 30: Psuedo-transfer function amplitude vs 27N frequency, 27-vane configuration

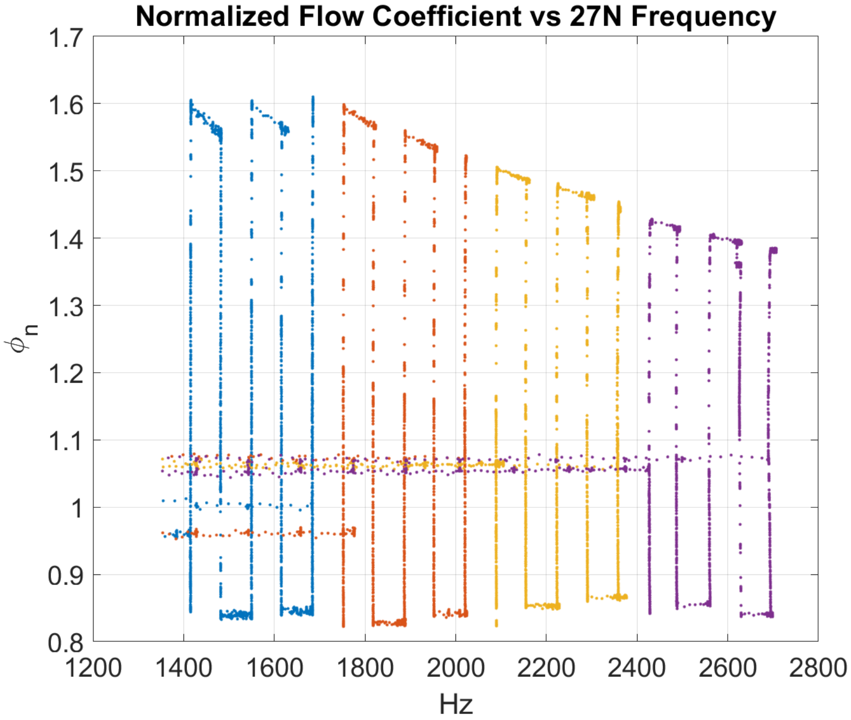

Figure 31: Normalized flow coefficient vs 27N frequency, 27-vane flow sweep configuration

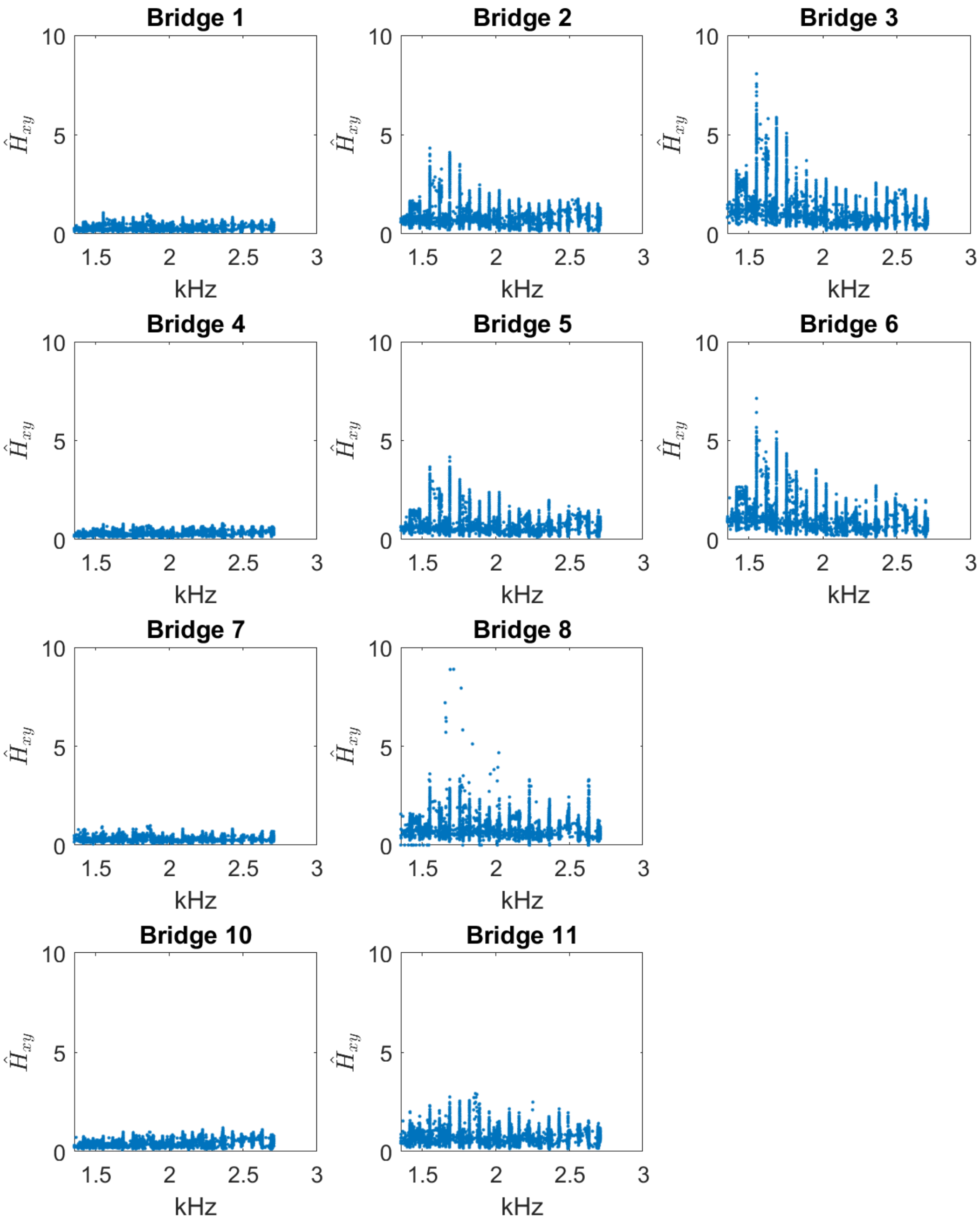

Figure 32: Psuedo-transfer function amplitude, 27-vane flow sweep configuration, all trackings